


REVIEW

[View Article Online](#)
[View Journal](#) | [View Issue](#)Cite this: *Mater. Horiz.*, 2025,
12, 5513Received 11th March 2025,
Accepted 3rd April 2025

DOI: 10.1039/d5mh00434a

rsc.li/materials-horizonsSilicon anode modification strategies in
solid-state lithium-ion batteriesYang Deng,^a Xiaohan Feng,^a Zhonglin Qian,^a Jurui Ma,^a Yitao Ouyang,^a Weijie Li^b and Chao Han^b  ^{*,a}

The development and application of solid-state electrolytes in lithium-ion batteries (LIBs) have become mainstream in the industry of LIBs. Compared with liquid electrolytes, solid-state electrolytes offer higher safety and energy density and are expected to further broaden the application fields of lithium-ion batteries. Conventional solid-state lithium-ion batteries (SSLIBs) employ lithium metal as their anode, which raises new concerns about their safety and waste management. Therefore, silicon, with high safety, high theoretical capacity, low electrochemical plateau, and low handle cost, has become the most promising new-generation anode material. However, due to the volume expansion of silicon and the low contact with solid-state electrolytes, resulting in poor conductivity, the SSLIBs' capacity has not reached the expected level and the cycle performance is also poor. Therefore, further modification of silicon anodes has become one of the key points in the development of SSLIBs. This paper comprehensively expounds on the application and optimization of silicon anodes in SSLIBs. It proposes further optimization strategies, which focus on preventing the destruction of silicon and extending its lifespan. The strategies include (1) silicon with different morphologies; (2) the formation of amorphous silicon; and (3) silicon composites.

Wider impact

This review discusses key developments of silicon anodes in solid-state batteries (SSBs) as the replacement of liquid electrolytes with solid ones is an unstoppable trend in the industry. Compared with traditional lithium metal anodes in SSBs, Si anodes in SSBs have advantages like lower dendrite formation chance, decreased cost, and higher safety but also face issues like volume expansion, low conductivity and electrochemical sintering. The area is of wide interest due to the potential of SSBs in energy storage. The future holds the need for strategies to enhance Si anode performance in SSBs. Previous related pioneering reviews focus mainly on demonstrating the performance of silicon anodes in SSBs. In contrast, this review offers a more comprehensive analysis of Si-based anodes in SSBs, summarizing performance enhancement strategies, which can guide the development of materials in materials science for better energy storage solutions.

Introduction

Liquid electrolyte based lithium-ion batteries (LELIBs) are widely used as a power source for portable electronic devices due to their high ionic conductivity, low cost, high energy density, high power density, and long cycle life.^{1–4} However, some disadvantages such as poor security, unsatisfying charging rate, and high sensitivity to temperature still exist.^{5–8} To address the main drawbacks of traditional lithium-ion batteries, researchers propose to employ solid-state lithium-ion

batteries (SSLIBs) as an effective strategy to improve the defects of lithium-ion batteries. In contrast to traditional lithium-ion batteries, which use organic liquids, SSLIBs use polymer or inorganic solid electrolytes. These solid-state electrolytes (SSE), especially inorganic ones, provide significantly enhanced thermal stability, which minimizes the risk of fire and explosion, enabling safer and more stable battery designs, which are essential for applications that require high reliability, including transportation systems such as electric vehicles, and a wide range of energy storage solutions. In addition, solid-state electrolytes provide higher energy density compared to liquid electrolytes and they can be easily encapsulated. Unlike liquid batteries, which require a separator to prevent short circuits, solid-state electrolytes do not require a separator for ion transport, and the higher mechanical strength is sufficient to inhibit

^a School of Materials Science and Engineering, Central South University, Changsha 410083, Hunan, P. R. China^b Powder Metallurgy Research Institute, Central South University, Changsha 410083, Hunan, P. R. China

lithium dendrite growth and extend battery life. It is common sense that the solid-state electrolyte is a breakthrough in the field of lithium-ion battery energy storage, and the replacement of liquid electrolytes by solid-state electrolytes is the unstoppable trend of lithium-ion battery energy storage development.

With a low charging and discharging platform (under -3.04 V vs. standard hydrogen electrode, SHE) and high theoretical capacity (3860 mA h g^{-1}), lithium has been thought as the first choice for the negative electrode of SSBs due to its low fabrication cost.^{9–11} Unfortunately, at this stage some problems still hinder the further application of lithium as negative electrode material: the huge volume expansion during stripping/plating is unavoidable, leading to interface contact or stress accumulation problems; the excess amount of Li counteracts its high safety.^{12–15} For example, Atul Kumar Mishra *et al.* reported that at the interface between the lithium metal anode and the solid-state electrolyte, lithium dendrites could nucleate and grow at an extremely rapid rate, posing a significant threat to battery performance and safety.¹⁶ In addition to lithium metal anodes, carbon-based anodes, lithium titanate anodes and silicon-based anodes have been one of the research hot-spots. Carbon-based anodes, with graphite anode being the typical example, currently dominate large-scale commercial anode materials, but their theoretical specific capacity is only 373 mA h g^{-1} , which is far lower than that of silicon anodes (4200 mA h g^{-1}); as a result, it is difficult for graphite anodes to meet the energy supply requirements of future portable electronic devices. The lithium titanate anode has a stable lattice and a three-dimensional ion diffusion channel owing to the spinel structure of lithium titanate, so it meets the high rate, long span life and safety requirement, but the theoretical capacity of lithium titanate is only 176 mA h g^{-1} , which is difficult to achieve a high capacity density of lithium-ion batteries. So, as is the case with LELIB, silicon is again emerging as a potential anode to replace anode materials such as lithium metal. Therefore, similar to the advancements in

LELIBs, silicon has re-emerged as a promising negative electrode material, offering a potential alternative to lithium metal in solid-state batteries. For one thing, Si has high theoretical lithium storage capacity and low cost. For another, the lithium storage voltage of silicon is higher than that of lithium metal, reducing the formation chance of lithium dendrites. At last, the replacement of lithium metal using silicon increases battery safety and further cuts the fabrication cost.^{17–20} Furthermore, due to the existence of external stack pressure or stress in SSBs and less exposure chance between Si and the solid-state electrolytes, Si anodes in SSBs could show less particle pulverization. It is highly expected that problems encountered in LELIBs would be partially suppressed by the SSLIBs, and the capacity and longevity of the battery would be therefore improved. Jaewon Kim *et al.* proposed that after battery manufacturing, a specialized device is used to maintain a constant pressure, called stack pressure, which promotes contact between Si and SSE, which not only effectively alleviates the expansion of Si, but also improves the conductivity due to the shortening of the lithium ion transmission distance, leading to high battery performance.²¹ Specifically, Mari Yamamoto *et al.* applied different stacking pressures to Si anodes used in solid-state batteries, and found that a larger compression pressure could prevent the formation of silicon particle cracks and repair small cracks, and also caused small-scale plastic deformation in Si and SSE to promote closer contact, and at the same time, after a long period of cycling, it was observed that vertical cracks were formed, and were quickly closed due to the expansion of silicon, and by repeatedly opening and closing the cracks in the same position, the expansion stress of Si was relieved, promoting circulatory stability.²²

However, silicon-based materials still face many problems:

(1) Like in LELIBs, the silicon material undergoes an unavoidable huge volume expansion ($\sim 400\%$) during the lithiation process, resulting in cracking and pulverization, which reduces its electrochemical performance and causes instability for the whole SSBs.^{23,24}



Yang Deng

Y. Deng is a junior undergraduate student at the School of Materials Science and Engineering, at Central South University. He is focused on improvement strategies for silicon anodes in solid-state lithium-ion batteries and the regulation of lithium deposition in lithium-metal batteries.



Chao Han

Prof. Chao Han received his bachelor's and master's degrees from Central South University and obtained his PhD from the University of Wollongong, Australia, in 2016. He joined the School of Materials Science and Engineering at Central South University in 2022 and was awarded the National Overseas Young Talent Program in 2023. His research focuses on developing cost-effective metal/metal chalcogenide-based functional materials through powder metallurgy methods, with primary applications in electrocatalysis, electrochemical and thermoelectric technology.

(2) The low conductivity (compared with lithium metal) of silicon still affects the electrochemical performance of SSBs.^{25,26}

(3) Electrochemical sintering occurs. The stress from the lithiation process makes it possible for adjacent Si atoms from different particles to form new chemical bonds, resulting in the merging of two particles into a larger one; consequently, the advantage of small size is lost and local expansion is increased. As this process is related to the electrochemical process, it is defined as electrochemical sintering. For example, Ryoshi Ohta reported that the small size of Si nanoparticles within the electrode formed a grid-like structure, and although this maintained contact with SSE, a greater external pressure was required to prevent cracking, and that Si particles larger than 150 nm in size exhibit a large initial capacity and a small charge transfer resistance, but a continuous attenuation of capacity was observed during long cycles, resulting from vertical cracking of large Si grains that were deformed and merged.²⁷ This phenomenon is less severe in LELIBs due to the low stress states in the electrode, while for SSBs, the externally applied pressure promotes a greater degree of contact between Si particles, which are prone to form larger particles, and the volume expansion generated during the lithiation process greatly affects the cycle life of the battery.

To sum up, investigating the performance of silicon anodes in SSBs is of great meaning and could promote the application of SSBs in the future. However, there is no specific review on this topic.

Liu *et al.* introduced the development of silicon-based anodes in LIBs and introduced the application of silicon in solid-state lithium-ion batteries as electrolytes evolved from liquid to quasi-solid-state and eventually to all-solid-state electrolytes.²⁸ In terms of the compatibility of solid-state electrolytes with silicon anodes, Sun *et al.* outlined the key research directions and latest breakthroughs in the integration of silicon-based anodes into SSB systems.²⁹ However, these pioneering works focus more on the performance of the silicon anode and lack detailed strategies for performance enhancement.

Therefore, given the above challenges and as depicted in Fig. 1, we undertake a more comprehensive analysis of Si-based anodes in SSBs, focusing on the electrochemical-mechanical behaviors of Si-based materials and structural changes that occur at the microscopic and mesoscopic scales in SSBs, analyzing the effects of different aspects on the electrochemical performance of silicon anodes. Particularly, we pay attention to summarizing the strategies to further enhance the electrochemical performance of silicon anodes in SSBs.

Strategies for improving the electrochemical performance of silicon anodes in SSBs

Due to the high potential of silicon, silicon-based anode materials, including both pure silicon and silicon-based

composites, have been explored as negative electrodes in SSBs. According to the properties of different Si based materials, many strategies aiming to alleviate the volume expansion of silicon during cycling to obtain better electrochemical performance are proposed.^{30,31}

Silicon with different morphologies

Inspired by the situation in LELIBs, wherein various well-designed nanostructures have been successfully applied, the volume expansion of silicon could also be suppressed in SSBs. While stack pressure application offers a partial solution, optimizing nanostructural design remains a critical strategy for enhancing the performance of SSBs.^{32–34}

Silicon nanoparticles

Current research has proved that when reducing the size of silicon to the nanoscale, due to the increase of specific surface area, the surface stress of the particles will be reduced, which can alleviate the volume expansion of silicon; in addition, because the lithium ion transport path is also shortened in the nanostructure, it is also beneficial to battery kinetics. Therefore, structures such as silicon nanoparticles, nanowires, and nanotubes have aroused the interest of researchers. However, the contact of nanoparticles with the solid electrolyte in the battery is rather limited, which diminishes the capacity and conductivity.³⁵ Relevant studies have shown that micro-sized particles are in better contact with the solid electrolyte, resulting in better capacity and conductivity, while the surface stress is even more deadly because of larger volume and less specific surface area, causing the tendency to fragmentation. Therefore, scientists have begun to mix nanoscale and microscale Si particles.

Masanobu Chiku *et al.* have reported the electrochemical performance of microscale Si (m Si) and nanoscale Si (n Si) in SSBs (Fig. 2a and b). During cycling, m Si provides a high initial discharge capacity of 2400 mA h g⁻¹ (Fig. 2c). However, due to significant volume changes during the charge/discharge process, m Si particles developed cracks and voids, which disrupted the ion and electron conduction pathways. This resulted in a rapid decrease in capacity over successive cycles. In contrast, n Si exhibited a lower initial discharge capacity of 1000 mA h g⁻¹ (Fig. 2d), while demonstrating an increase in capacity during the first 20 cycles, the reason for which is better contact with the solid electrolyte, as the smaller size of n Si reduces the formation of cracking and maintains the structural integrity of the electrode. By mixing m Si and n Si in a 7 : 3 mass ratio, the combination achieved complementary benefits. The mixture harnessed the high initial capacity of m Si and the longer cycle life of n Si. This ratio optimized the balance between maximum discharge capacity and capacity retention. The mixture showed an initial discharge capacity exceeding that of both pure m Si and n Si electrodes, with improved cycle stability. The capacity retention after 200 cycles was around 72%, compared to 39% for m Si alone and 85% for n Si alone.³⁶

Besides simple and low-cost mixing of nano- and micro-scale structures, morphology engineering of the nanostructures

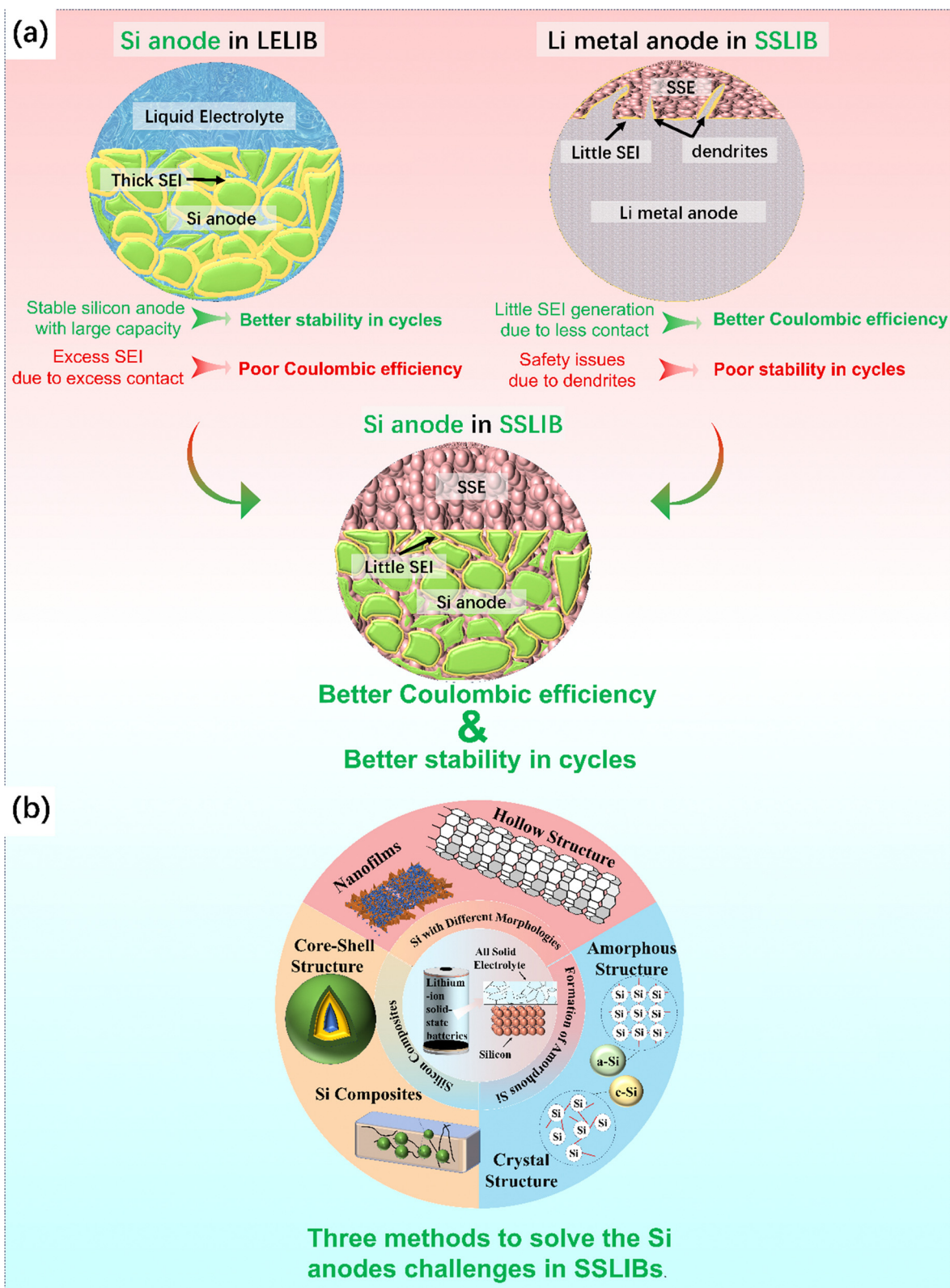


Fig. 1 (a) Advantages of Si anodes in SSLIBs and (b) three methods to solve the challenges of Si anodes in SSLIBs.

is also effective. For example, Zhang *et al.* encapsulated Si in a B–C framework by sol–gel and annealing methods, and then combined it with reduced graphene oxide (rGO) through

ultrasonic and centrifugal treatments, obtaining Si@B–C/rGO nanomaterials. The nanoparticles maintained a regular spherical structure and were eventually distributed on rGO

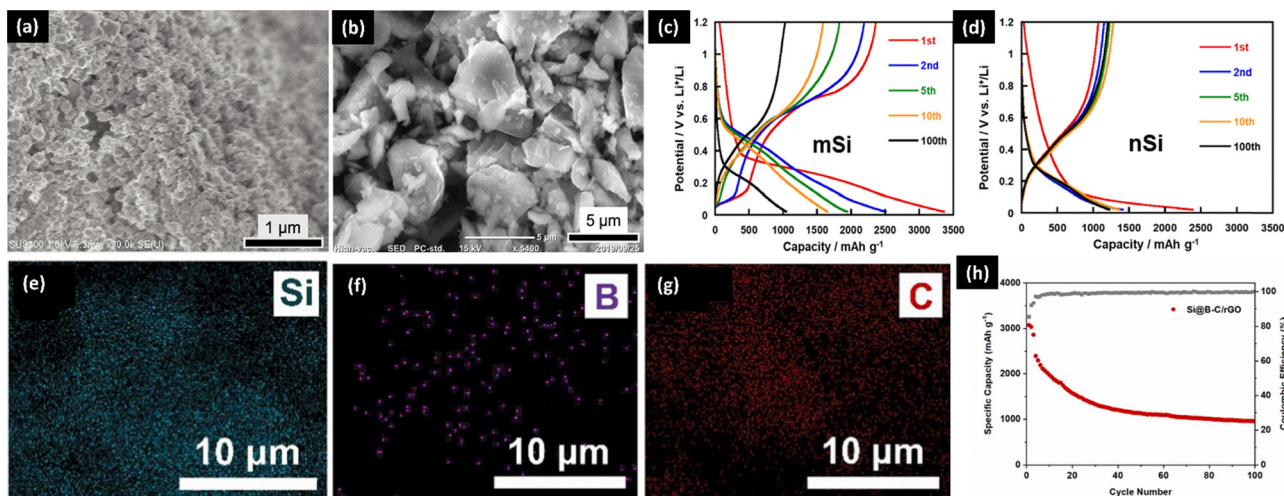


Fig. 2 (a) SEM images of n Si. (b) SEM images of m Si. (c) The charge/discharge curve of m Si. (d) The charge/discharge curve of n Si. Reproduced with permission.³⁶ Copyright 2024 Elsevier. (e)–(g) Corresponding EDS maps of Si@B-C/rGO. (h) Cycle performance of Si@B-C/rGO in an all-solid-state battery at 0.1 mA cm⁻². Reproduced with permission.³⁷ Copyright 2024 Elsevier.

(Fig. 2e–g), and the specific surface area reached 95.91 cm² g⁻¹. This can reduce particle aggregation, promote the transmission of lithium ions, and also enhance mechanical strength, and suppress volume expansion. In solid-state batteries, this electrode material exhibited an initial coulombic efficiency of 85.6%, and after 100 cycles at 0.1 mA g⁻¹, the capacity remained at 956 mA h g⁻¹ (Fig. 2h). However, in the liquid electrolyte under the same conditions, the specific capacity of the battery after 100 cycles can always reach above 1000 mA h g⁻¹; this might be caused by the restricted ion transport in the solid state.³⁷

As mentioned above, the key to improving the performance of solid-state batteries is to maintain long-period stable contact between the Si anode and SSE, and at the same time, prevent

the agglomeration of Si nanoparticles during cycling to avoid the occurrence of electrochemical sintering. Jeongheon Kim *et al.* encapsulated Si nanoparticles in carbon nanofibers (CNF) by a simple electrospinning method and coated a layer of lithium phosphorus sulfur chloride (LPSCl) solid electrolyte by a liquid-phase method to obtain Si/CNF@LPSCl anode material. Embedding Si nanoparticles into CNF ensures a uniform distribution of Si and avoids agglomeration (Fig. 3a and b). This structure helps to achieve an efficient release of stress while maintaining the density of the structure (Fig. 3c and d), thus ensuring the stability of electron transport. In addition, this material reduced the amount of solid electrolyte in the electrode without significant performance loss, achieving an increase in energy density and a cost reduction. At a charge–

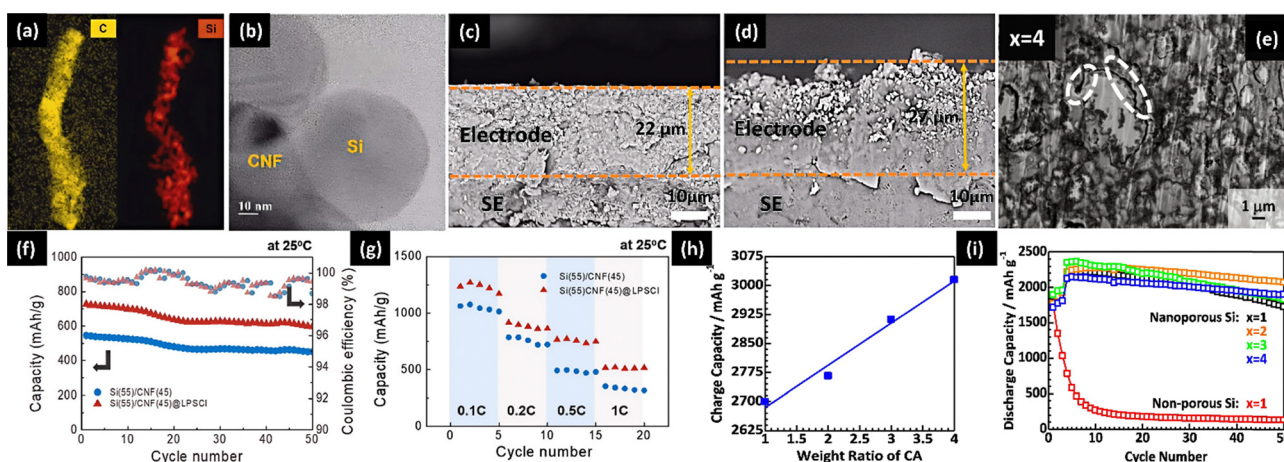


Fig. 3 (a) EDS mapping of the Si/CNF composite. (b) HR-TEM image of the Si/CNF composite. (c) SEM image of the cross-section of the Si/CNF@LPSCl composite before cycling. (d) SEM image of the cross-section of the Si/CNF@LPSCl composite after cycling. (e) Cross-sectional FE-SEM images of nanoporous Si half-cells containing various amounts of CA. (f) Cycle performance of the Si/CNF composite electrode and Si/CNF@LPSCl composite electrode at 0.5C rate. (g) The rate capability of the Si/CNF composite electrode and Si/CNF@LPSCl composite electrode. (h) *I*–*V* Characteristics of nanoporous Si half-cells containing different amounts of CA. (i) Initial charge/discharge curves of nanoporous Si half-cells containing various amounts of CA. Reproduced with permission.^{23,38} Copyright 2021 Elsevier. Copyright 2022 Elsevier.

Table 1 Modification scheme and electrochemical performance of silicon nanoparticles

Si-based anode	Electrolyte	Initial CE	Specific capacity (mA h g ⁻¹)	Current	Initial discharge capacity (mA h g ⁻¹)	Ref.
Micro- and nanoparticle mixtures	Li ₂ S–P ₂ S ₅	~ 99%	1000 (200 cycles)	120 mA g ⁻¹	2400	36
Si@B–C/rGO	—	85.60%	956 (100 cycles)	100 mA g ⁻¹	~ 3050	37
Si/CNF@LPSCI	LPSCI	89.60%	~ 1027 (50 cycles)	0.5C	1218	23
CA composite anode	—	91.00%	2071 (50 cycles)	0.03C	~ 2277	38

discharge rate of 0.1C, this electrode exhibited a high reversible capacity of 1218 mA h g⁻¹ (Fig. 3g), and after 50 cycles at a rate of 0.5C, it could maintain 84.3% of its capacity (Fig. 3f). However, since the high carbon content of the material reduces the proportion of active material silicon, it is difficult to achieve the high lithium storage capacity of silicon.²³ Ryota Okuno and others used ball milling to mix nanoporous silicon particles, Li₃PS₄ solid electrolyte, and conductive additives in a certain weight ratio to prepare composite anode materials. The introduction of nanoporous silicon particles effectively alleviated the volume expansion problem of silicon during charging and discharging, improving the cycle stability of the battery. By adding a suitable proportion of CA, the silicon particles were effectively separated preventing agglomeration and electrical loss, and new conductive paths were formed, significantly improving the electrical conductivity and charge capacity (Fig. 3h). The capacity retention rate of the nanoporous silicon half-cell after 50 cycles was as high as 91%, and the discharge capacity reached 2071 mA h g⁻¹ (Fig. 3i). Although the nanoporous structure can alleviate silicon expansion, cracks can still be seen between the silicon aggregates and the electrolyte under the highly conductive additive (Fig. 3e). The content and distribution of additives should be further optimized to balance the conductivity and structural stability.³⁸

In general, nanostructured Si particles are seen as an excellent solution to the Si anode challenges in SSLIBs, but the process needs to be carefully selected, and the convenient and simple mechanical ball milling method is generally chosen, and the expected size can be achieved through strict control of the ball milling speed and time, which may require multiple attempts to gain experience.

Concurrently, to prevent the electrochemical sintering of fine silicon particles, which could lead to the formation of excessively large particles, while ensuring an adequate degree of contact between silicon and the electrolyte, it is customary to employ methodologies such as encapsulation and modification. These approaches are instrumental in prolonging the lifespan of the anode, and the relevant data can be found in Table 1.

Silicon nanofilm

Compared with the three-dimensional structure, the size of the two-dimensional structure in one direction is extremely small, so the volume expansion only occurs in the two-dimensional plane, which greatly reduces the risk of pulverization, and therefore, the two-dimensional silicon-based anode shows better stability. However, due to the blockage of lithium ions

and electron transport between solid-state interfaces, more conductive agents need to be added to form a conductive network.

Xin Li *et al.* prepared a carbon interconnected micro-sized Si film (MSi–C) by ball mill mixing micron-sized silicon (MSi) powders with an average diameter of ~1.5 μm and polyacrylonitrile (PAN) and then calcining at 700 °C for 2 h. As shown in Fig. 5a, the MSi particles are embedded in a network of carbonized PAN films. During the thermal heating process, a thin layer of amorphous carbon is coated on the surface of the MSi, and there should be a strong interaction with each other; XRD shows that no diffraction peak of graphite is detected, implying that the carbon is amorphous (Fig. 4a).

Carbon enhances the mechanical properties and conductivity of the anode due to its high binding and conductivity properties; in addition, it promotes the formation of a LiF-rich and electrochemically stable solid-electrolyte interphase (SEI) layer. As shown in Fig. 4b, when applying a high-rate current density of 1 A g⁻¹, the MSi–C anode provides a specific capacity of 2131 mA h g⁻¹. In the first 100 cycles, the battery showed stable cycling performance, with a slight increase in capacity to a value of 2327 mA h g⁻¹. After that, the MSi–C electrode slowly decays and retains a specific capacity of 1135 mA h g⁻¹ after 500 cycles, which corresponds to a capacity retention rate of 53%. Fig. 4c shows the rate performance of MSi–C in a solid-state battery at different current densities of 0.5, 1, 2, and 3 A g⁻¹, with specific capacities of 2137, 2078, 1971, and 1793 mA h g⁻¹.³⁹

Due to the contact between the two-dimensional negative electrode and the solid electrolyte, which has a larger specific surface area, the volume expansion is more severe, and existing studies have shown that the structure with a more complex curvature can help disperse the stress field and mitigate the effects of expansion. Rui Qiao *et al.* designed an innovative silicon thin-layer structure, which is combined into an independent silicon graphite composite integrated (SGCI) anode by a facile one-pot sintering. As shown in Fig. 5d, a layer of silicon adheres to the pitch, and the excellent compressive strength of the pitch makes it have a strong resistance to deformation, so that the electrode can maintain high density and less expansion during the cycle. Comparing the SEM images before and after the cycles, it can be seen that the ordinary Si/C electrode shows obvious cracks after 50 cycles, while the SGCI electrode still exhibits a significant porous structure, indicating structural stability during circulation. In electrochemical tests, the high initial coulombic efficiency (ICE, 88.8%) indicates that the SGCI electrode can achieve more complete lithiation/delithiation. The rapid increase in CE in subsequent cycles (> 99% after

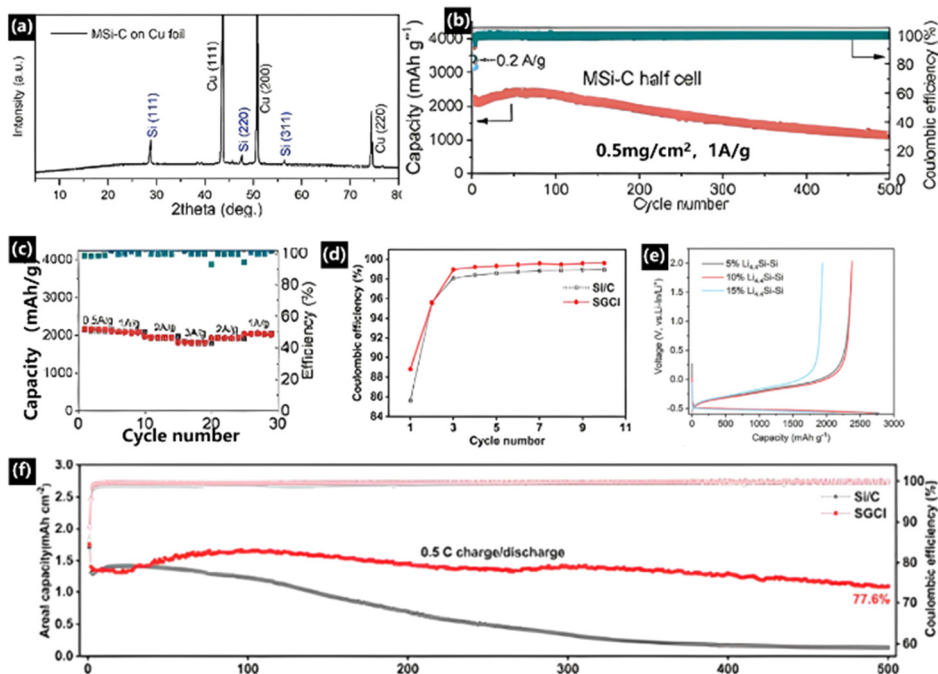


Fig. 4 (a) XRD patterns of the MSI-C anode. (b) The long-term cycling performance of MSI-C. (c) The rate performance of MSI-C in a solid-state cell. Reproduced with permission.³⁹ Copyright 2025 Elsevier. (d) Coulombic efficiency changes of Si/C and SGCI electrodes within 10 cycles. Reproduced with permission.⁴⁰ Copyright 2024 ACS publication. (e) Initial cycle voltage profiles of the $\text{Li}_{4.4}\text{Si-nSi}$ half-cells with different amounts of $\text{Li}_{4.4}\text{Si}$. Reproduced with permission.⁴¹ Copyright 2024 John Wiley and Sons. (f) Cycling performance of Si/C and SGCI electrodes over 500 cycles with mass loadings of 1.53 and 1.51 mg cm^{-2} at 0.5C ($1\text{C} = 1000 \text{ mA g}^{-1}$). Reproduced with permission.⁴⁰ Copyright 2024 ACS publication.

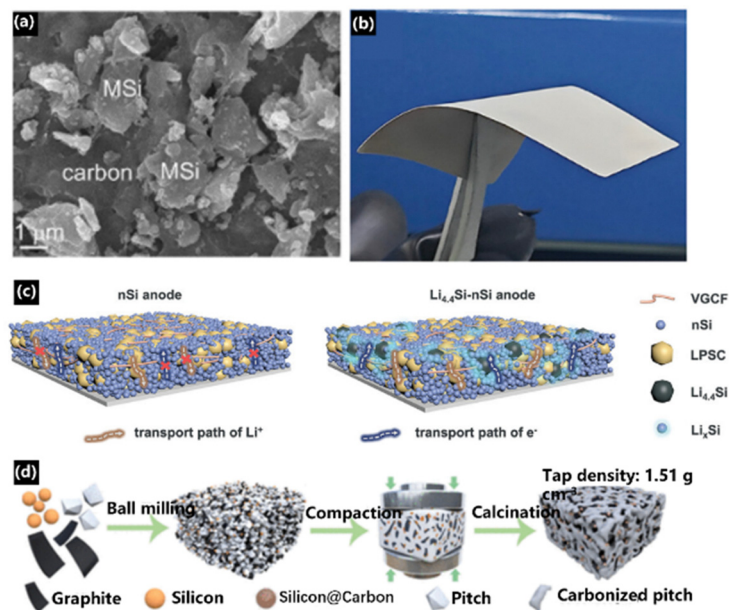


Fig. 5 (a) Surface SEM image of the MSI-C electrode. Reproduced with permission.³⁹ Copyright 2025 Chinese Chemical Society publication. (b) Digital picture of the LPSC membrane. (c) Schematic of the nSi anode compared with $\text{Li}_{4.4}\text{Si-nSi}$ anode design. Reproduced with permission.⁴¹ Copyright 2024 John Wiley and Sons. (d) Preparation of the SGCI electrode. Reproduced with permission.⁴⁰ Copyright 2024 ACS publication.

four cycles) indicated that the binder-free SGCI electrode inhibited side reactions with the electrolyte (Fig. 4d), while the SGCI electrode maintained a high capacity retention rate of

77.6% after 500 cycles at 0.5C (Fig. 4f), and the long cycle life of the battery also indicated the high stability of the electrode structure.⁴⁰

Two-dimensional structure plus pre-lithiation can further diminish the volume expansion. Shenghao Jing *et al.* prepared a two-dimensional flake s-Li_{4.4}Si-nSi anode for all-solid-state lithium-ion batteries by ball milling Li_{4.4}Si and silicon nanoparticles (nSi), in which Li_{4.4}Si can not only provide additional lithium, but also stabilize the anode structure with a low Young's modulus during cycling. Fig. 5b and the electrochemical impedance spectroscopy (EIS) results show that the Li transport capacity of nSi is significantly lower than that of Li_{4.4}Si-nSi (Fig. 4e). This is because the particle size of nSi is much smaller than that of Li₆PS₅Cl (LPSC), and the LPSC particles are surrounded by nSi in the original anode, which makes it difficult for the LPSC particles to form an efficient lithium transport network. With the addition of Li_{4.4}Si, it is dispersed around nSi and interacts with nSi during the preparation of composite anode sheets and the subsequent high-voltage operation (Fig. 5c). In the electrochemical test, Li_{4.4}Si-nSi showed excellent stability, with a capacity retention rate of 96.16% after 100 cycles at 0.5 C, which was significantly improved compared to nSi (53.47%).⁴¹

In conclusion, the construction of a two-dimensional Si thin film structure at the level of nanostructure achieves small-scale volume expansion, which effectively solves the challenges faced by the Si anode in SSLIBs, and because the thin film layer provides a shorter ion transport channel, and the unique two-dimensional structure makes the conductive network easier to form, it also greatly contributes to the conductivity of the Si-based anode. In the process of preparing 2D nanofilms, ball milling and pressure processing can effectively control the morphology and size of the sample, and the specific experimental data are listed in Table 2.^{42–45}

Silicon hollow structure

In view of the shortcomings of the relatively weak strength of the nanofilm structure, researchers proposed a hollow nanos-structure, which can withstand much more stress due to its larger cross-sectional area and has higher mechanical strength; the expansion of Si both in the wall and into the hollow interior mirrored that of a nanofilm structure to achieve the effect of relieving stress.

Ryota Okuno *et al.* prepared porous Si by air oxidation of MgSi₂ by the air oxidation method. As shown in Fig. 6a and b, disordered nanometer pores are observed in SEM and TEM images, demonstrating the successful preparation of porous nano-Si particles. As shown in Fig. 6c, the porous Si nanoparticles are highly dispersed in the solid electrolyte matrix, although due to the large interface area between the solid electrolyte and Si particles, it is possible to form a surface

electrolyte interface (SEI) in the electrode, resulting in low initial coulombic efficiency (ICE), as it is expected, with a considerable number of exposed pores mitigating the large volume changes during lithiation and decalcification. As a result, the ball-milled porous Si composite anode shows surprisingly high capacity retention, still maintaining more than 90% capacity retention after 100 cycles (Fig. 6d).⁴⁶

The relevant data are summarized in Table 3. Since it is difficult to make a hollow tubular structure of Si, and considering that carbon nanotubes are easy to obtain, it is possible to achieve a similar effect to Si nanotubes by evenly attaching Si to the inner and outer surfaces of carbon nanotubes.⁴⁷

In conclusion, various nano-scale silicon structures have been shown to be used as the anode of LIBs to participate in the cycle, with no fatal structural changes occurring, whereas due to the large specific surface area of the nanostructure, the formation of SEI is not negligible, and for larger structures, such as micron silicon particles, volume effects and crushing will affect the life of the anode. Therefore, researchers are committed to finding a balance between various silicon particle sizes to obtain an excellent specific capacity and coulombic efficiency.

Formation of amorphous silicon

Silicon could be classified into crystalline silicon (c-Si) and amorphous silicon (a-Si) according to the difference in the internal structure.⁴⁸ c-Si has an ordered structure while abundant crystal defects and dangling bonds appear in the structure of a-Si, which cause the atoms to deviate from their normal orbits, resulting in plenty of large gaps between atoms. Consequently, the lithiation process of c-Si is not exactly the same as that of a-Si. For c-Si, the process of lithiation and delithiation results in tremendous stress and volume expansion due to the ordered structure; in addition, the phase border moves at different rates in different directions during the lithiation process, resulting in irreversible anisotropic expansion. On the other hand, for a-Si, lithium ions lead to less expansion due to large gaps between atoms, and owing to the absence of crystal orientation and boundaries, the phase boundary moves isotropically, which is conducive to alleviating stress. As shown in Fig. 7a, Zhao *et al.* have reported that the dangling bonds existing in the amorphous silicon cause the gaps between Si atoms become larger, and these larger gaps provide more binding sites during cycles without tremendous cracking and pulverization. Therefore, decreasing the crystallinity or increasing the defect degree of the Si lattice by element doping has become another effective strategy to improve the performance of the silicon anode in SSBs.⁴⁸

Table 2 Preparation method and electrochemical properties of nanofilms

Si-based anode	Method	Electrolyte	ICE	Capacity retention	Current	Initial capacity	Ref.
MSi-C film	Ball milling and calcination	PVDF-HFP/LATP	83.2%	53.1% (500 cycles)	500 mA g ⁻¹	2137 mA h g ⁻¹	39
Si-graphite film	Facile one-pot sintering	Li ₆ PS ₅ Cl	88.8%	98.5% (1000 cycles)	0.5C	—	40
Li _{4.4} Si-nSi film	Ball mill mixing	Li ₆ PS ₅ Cl	—	96.16% (100 cycles) 70.03% (400 cycles)	0.5C	—	41

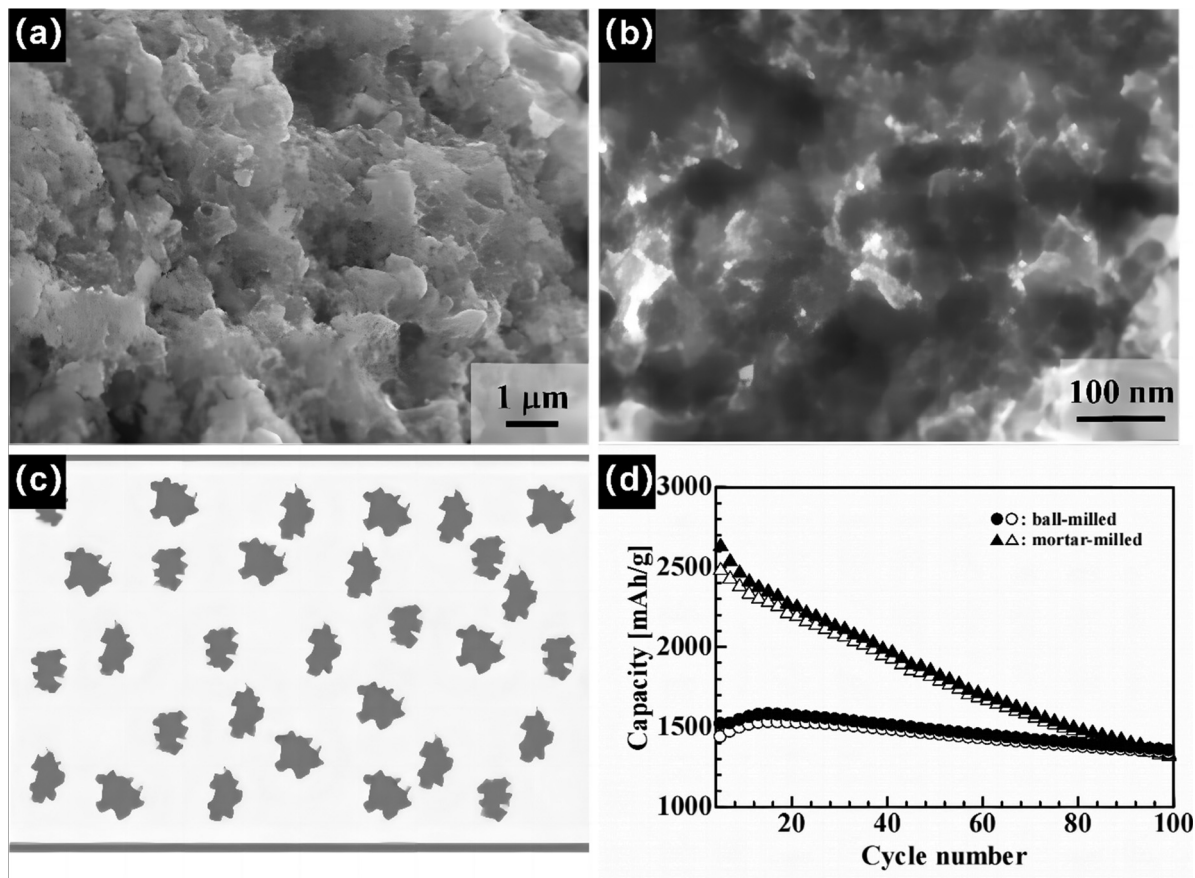


Fig. 6 (a) SEM and (b) TEM images of porous Si nanoparticles. (c) Structural models of ball-milled composite anodes. (d) Plot of discharge (filled) and charge (open) capacity versus cycle number of ball-milled (circle) porous Si composite anodes. Reproduced with permission.⁴⁶ Copyright 2019 Elsevier.

Table 3 Preparation method and electrochemical properties of the silicon hollow structure

Si-based anode	Method	Electrolyte	ICE	Capacity retention	Current density	Initial capacity	Ref.
Porous Si	Ball mill	Li ₃ PS ₄ glass	49%	93% (100 cycles)	0.3 mA cm ⁻²	1290 mA h g ⁻¹	46

Fan *et al.* employed the chemical vapor deposition (CVD) technique to deposit a gaseous silane coupling agent (KH569) onto a magnesium oxide template, followed by removing the template to yield SiO_xC_y microtubules (Fig. 9k). From the SEM and TEM images, it can be observed that the composite material has a rough and porous tubular structure with a thickness of 30 nm (Fig. 10a–c). This unique structure, combined with its amorphous nature, facilitates the mitigation of stress and strain during the lithiation/delithiation process, minimizing volume expansion and enhancing structural stability. The EDS mapping shows that O, C and Si are uniformly distributed in the material (Fig. 10d). Furthermore, the internal cavity of the SiO_xC_y tubules provides ample space for lithium deposition, while the uniformly distributed electric field ensures even deposition, effectively preventing the formation of lithium dendrites. Half-cells constructed with this material exhibit exceptional cycling performance, maintaining a high coulombic efficiency (CE) retention rate of 98.9% after 650 cycles at 1.0 mA cm⁻² (Fig. 10e) and achieving CE values

of 98.9% and 98.7% after 150 and 110 cycles respectively at 5.0 mA cm⁻² (Fig. 10f and g). However, the presence of excessive voids within the material, coupled with excessive carbon doping, can result in a reduction of Si content, subsequently decreasing the lithium storage capacity of the material and detrimentally impacting the battery's specific capacity, which is only 137 mA h g⁻¹ for 1C (Fig. 10h).⁴⁹

At the micro and mesoscopic scales, according to Zhao *et al.*, when considering silicon nanomaterials, amorphous structures are generally less prone to cracking than crystalline structures. However, the amorphization of silicon leads to worse electron conductivity. These properties provide an idea to reduce the swelling of silicon and increase the internal defects in the Si lattice, which could be viewed from both a micro and mesoscopic perspective. Especially when metal ions or non-metallic ions are doped into the lattice of crystalline silicon, lattice distortion will be triggered and suitable defects appear. By doping atoms of other sizes in the crystal lattice of Si, a local stress field will be caused, which causes a certain degree of

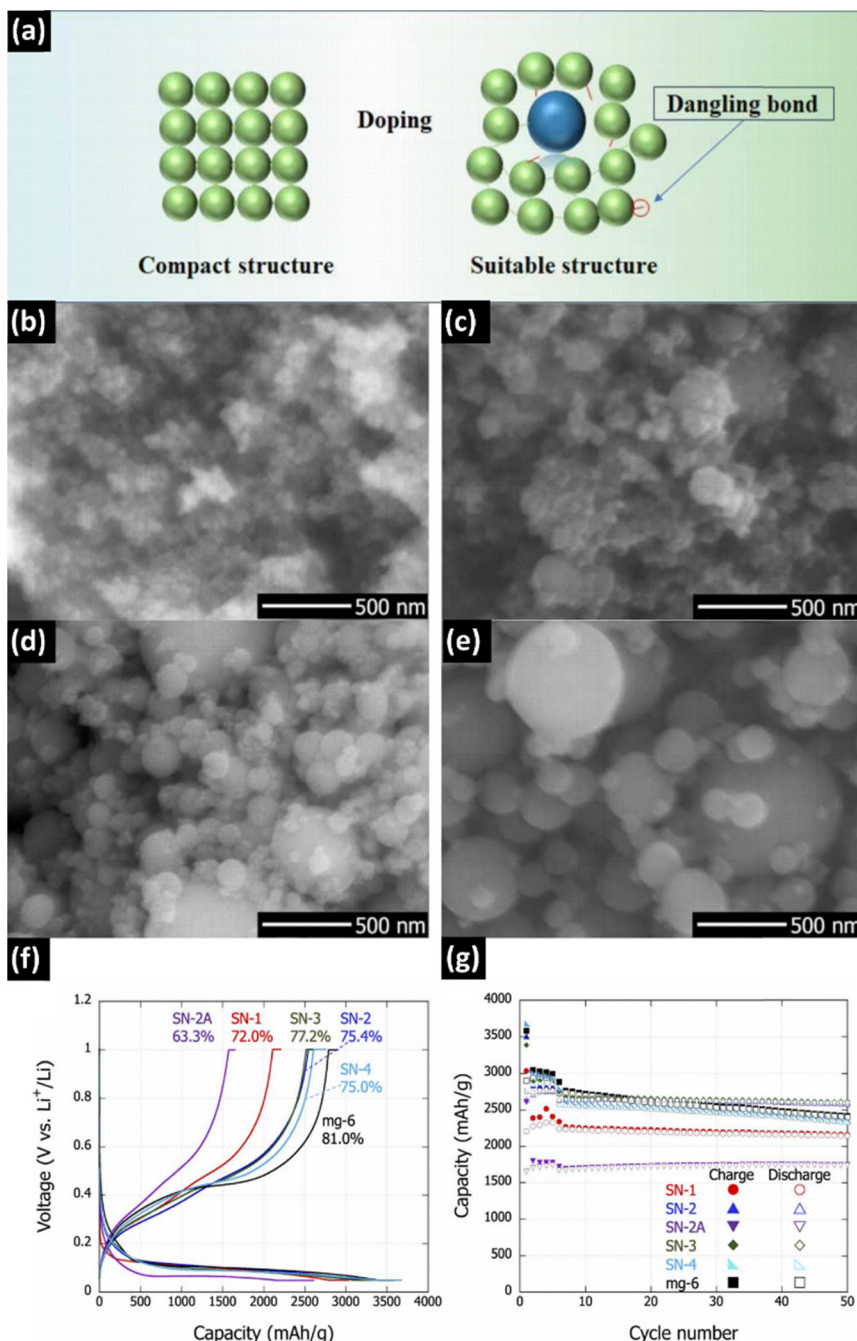


Fig. 7 (a) Illustration of the doping principle. (b)–(e) SEM images of SN-1, SN-2, SN-3, and SN-4. (f) Charge–discharge curves during the 1st cycle. (g) Cycle capacity of the cells using various Si particles. Reproduced with permission.²⁷ Copyright 2024 IOP Publishing.

distortion in the crystal lattice, and realizes the formation of increased lattice spacing and more dangling bonds. In addition, lattice distortion causes solution strengthening, which makes doped Si materials exhibit better mechanical strength and avoid destruction.

Non-metal element doping

Ryoshi *et al.* used the method of PS-PVD to control the degree of silicon oxidation by controlling the starting temperature and cooling rate of the reaction and obtained silicon nanoparticles

with different oxygen content (Fig. 7b–e). Compared to pure silicon, SiO_x experiences less volume fluctuation during charging and discharging, and cells utilizing SiO_x with an oxygen content below 0.1 can attain higher capacity and demonstrate exceptional cycling stability after 50 cycles. Specifically, they can sustain a capacity of approximately 2600 mA h g^{-1} at a rate of 0.02C over 50 cycles, with a coulombic efficiency of 99.5% (Fig. 7f and g). However, the presence of oxygen in the material will lead to irreversible passivation, which becomes part of the SEI passivation layer, resulting in a large capacity loss, so it is

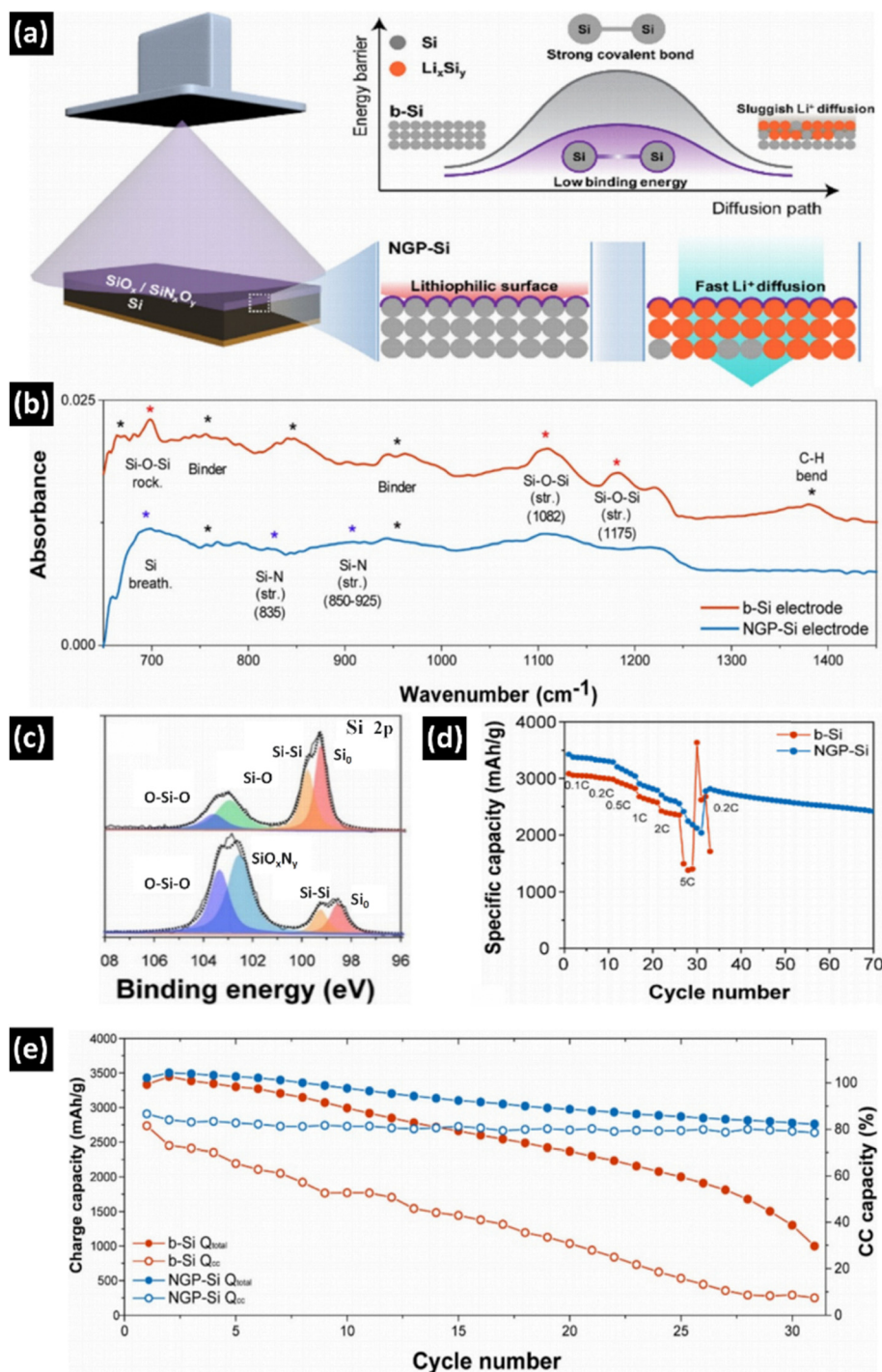


Fig. 8 (a) Illustration of NGP-Si anodes. (b) and (c) FT-IR and XPS analysis of Si 2p spectra of silicon electrodes before (top) and after (bottom) irradiating nitrogen plasma. (d) Rate capability test of the Si anodes with increasing current density from 0.1 to 5C. (e) An early phase of capacity decay and the percentage of CC capacity. Reproduced with permission.⁵⁰ Copyright 2022 ACS publication.

not suitable for practical applications.²⁷ However, PVD, as a widely used surface treatment technology, can oxidize the surface of Si particles or form an *in situ* film at a lower process temperature to achieve coating, which avoids the potential impact of excessive temperature on the Si lattice and meets the needs of large-scale production.

Su *et al.* treated a silicon electrode using a nitrogen plasma system and named it NGF-Si (Fig. 8a). FT-IR images reveal the formation of Si-N and Si-O-N bonds, which elevate the oxidation valence state of silicon, resulting in the production of more excess electrons (Fig. 8b). Furthermore, XPS analysis shows that nitrogen doping causes an increase in the Si-Si bond length

and a decrease in bond energy, favoring bond breakage (Fig. 8c). Consequently, the plasma-treated material surface lowers the energy barrier for lithium-ion diffusion, significantly enhances lithophilicity, and accelerates the charging and discharging processes. The composite materials exhibit discharge capacities of 2706 mA h g⁻¹ at 0.1C and 2413 mA h g⁻¹ at 5C, demonstrating robust performance even at high rates (Fig. 8d). After 30 cycles, the capacity retention rate remains at 78.6% and there is no significant capacity decline (Fig. 8e). However, NGF-Si fails to sustain its capacity during the charging and discharging cycles of solid-state batteries, undergoing rapid expansion, cracking, or even fracture, which leads to significant contact loss. Attempts to mitigate capacity loss by incorporating an equivalent amount of graphite into silicon were unsuccessful, as they led to a decline in electrochemical performance, with the cycle capacity being considerably lower than that of NGF-Si. Consequently, there is a necessary need to delve deeper into suitable treatment methods.⁵⁰

Ball-milling is a common process used to fabricate Si. On the one hand, ball milling can reduce the particle size of Si particles in a controlled and uniform manner to meet the needs of industrial large-scale production, and on the other hand, through the mechanical collision between high-speed balls and particles, great stress can be generated to introduce lattice defects, and inelastic collisions between different particles can also fuse smaller particles to form a unique doping structure. Lv *et al.* processed nano-Si particles derived from metallurgical silicon powder and phosphorus pentoxide through ball milling followed by treatment with HF to eliminate SiO₂ impurities, resulting in a highly porous P-doped material (Fig. 9a). SEM and TEM images reveal that the particle size is approximately 150 nm, exhibiting a stable mesoporous structure (Fig. 9b–d). With a raw material (SiO₂:P₂O₅) weight ratio of 10:2, the porosity of these particles reaches 45.8%, providing ample space to accommodate volume expansion and enhancing material stability (Fig. 9e). EDS images demonstrate that phosphorus was distributed throughout the particles, indicating effective doping (Fig. 9f and g). The incorporation of phosphorus significantly increases the conductivity by 10⁹ times, thereby boosting its electrochemical performance. After undergoing 940 cycles at 0.5C, the capacity remains stable at around 1500 mA h g⁻¹ (Fig. 9h). Additionally, its initial coulombic efficiency is 85.4% at 1C and remains above 99.1% after five cycles (Fig. 9i and j). However, the cycle count is relatively limited, and in the context of longer-term cycling, the pore structure could undergo alterations due to the insertion and extraction of lithium ions. Consequently, the material might encounter structural integrity issues, leading to capacity fading and performance deterioration.⁵¹

In the above analysis, the doping of non-metal elements in the lattice of Si is effective in increasing the atomic spacing and the formation of suspended bonds; however, with the same mass of electrode material, the Si-based material doped with some non-metal elements that cannot provide capacity (*e.g.*, N, O) or provide much less capacity (*e.g.*, C) exhibits a lower specific capacity than non-doped amorphous Si. It seems that

P is an ideal dopant, but its cycle performance still needs to be further improved.

Metal element doping

As most non-metal elements decrease capacity, existing studies have proven that metal ions can provide a certain capacity due to their ability to react with lithium, so the doping of metal elements with higher capacity (*e.g.*, Ag, V, Sn) further solves this problem.

Han *et al.* integrated high density Ag nanoparticles into three-dimensional porous microscale Si *via* a wet chemical etching method and encapsulated it by carbon coatings, fabricating a negative electrode material named PS-Ag-C (Fig. 11a). From the SEM, TEM and HAADF images, it is evident that the Ag nanoparticles are firmly attached to the PS matrix (Fig. 11b–e). Based on the BET analysis, the composites exhibit a diverse range of pore sizes, with an average pore diameter of 20.65 nm (Fig. 11f). Ag particles and the generated Li-Ag alloy can facilitate the promotion of electron mobility. Exploiting the reversible crystal characteristics of Ag, the cyclic formation of crystal Ag and Li-Ag alloy can reduce the nucleation energy of Li, which expedites the transport of lithium ions. The material exhibits a substantial reversible capacity of 3030 mA h g⁻¹ when tested at a current density of 0.2 A g⁻¹ and it can maintain a reversible capacity of more than 1600 mA h g⁻¹ at 1 A g⁻¹ after 500 cycles, with long-term cycle stability (Fig. 11g and h). However, due to the expensive price of Ag, the feasibility of this material in practical applications is low.⁵²

Luo *et al.* invented a silicon-based composite material, incorporating vanadium into silicon *via* a magnesium thermite reduction process, and subsequently covering its surface with a carbon layer, which is denoted as V-Si@C. As evident from the TEM images, the carbon coating on the material has a thickness of 50 nm, while the Si particles exhibit a diameter ranging approximately from 30 nm to 300 nm (Fig. 11i). Both TEM and EDS elemental mapping images of the material indicate a uniform distribution of vanadium within the silicon (Fig. 11j). The incorporation of vanadium not only increases the defect density and provides more active sites, but also leads to an expansion of the lattice spacing to 0.314 nm due to the introduction of a larger atomic species (Fig. 11k and l). This improves the transport efficiency of electrons and lithium ions, the latter of which plays a prominent role in enhancing the structural stability of the material. During 600 cycles under the condition of 1 A g⁻¹, the capacity keeps increasing and finally reaches 1216 mA h g⁻¹ (Fig. 12a). Nevertheless, V is not directly involved in the lithiation/delithiation process, and this will lead to a partial loss of capacity.⁵³

Mishra *et al.* decided to incorporate Ge, which shares analogous chemical characteristics with silicon, into its structure. The process involves mixing Si and Ge powders with 2 wt% boron powder, sonicating the mixture in isopropanol, then drying and heat-treating it to produce a uniform single-phase solid solution with particles averaging 0.3–0.5 μm, as indicated by the SEM images (Fig. 12b and c). The incorporation of larger-sized Ge will generate compressive stress, thereby

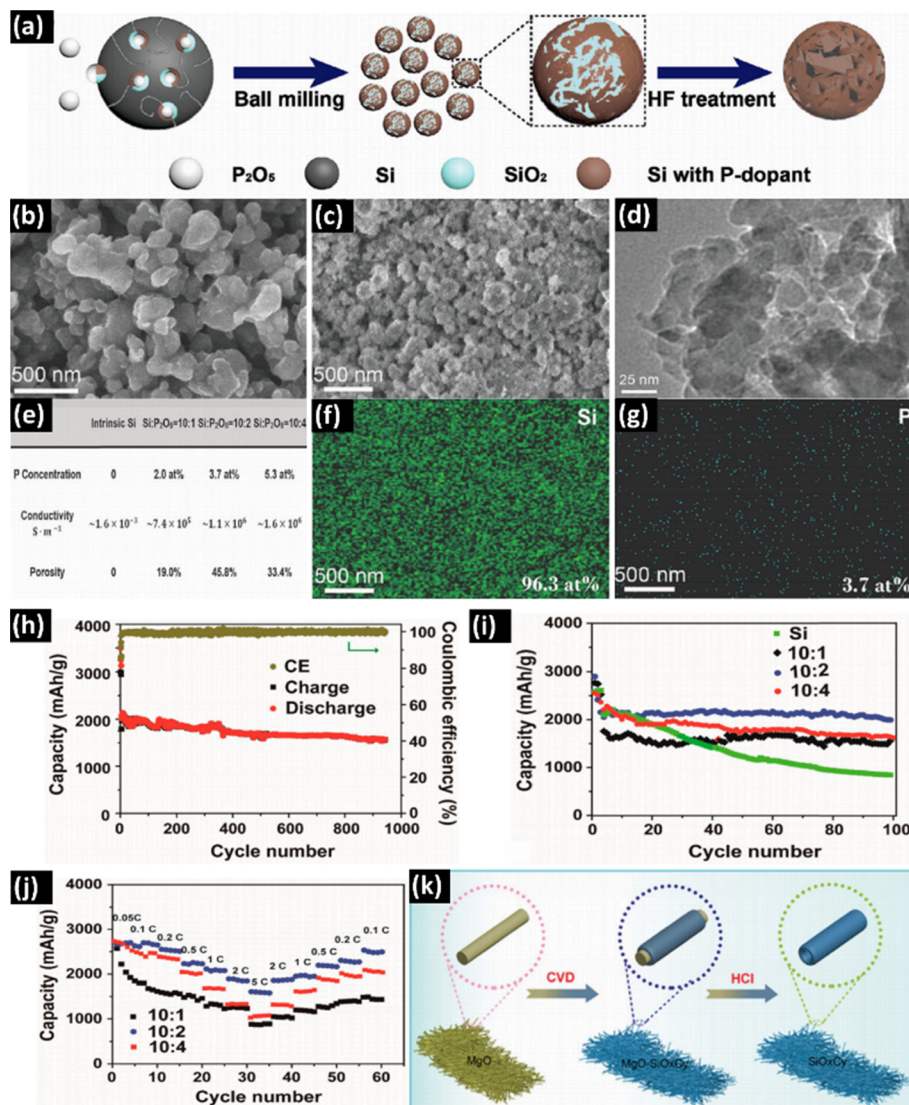


Fig. 9 (a) Schematics of the process containing two steps: high energy mechanical milling of Si and P_2O_5 , and hydrofluoric acid (HF) treatment. (b) SEM image of nano-Si particles with P-dopant and SiO_2 produced after ball-milling. (c) SEM image of P_2O_5 powders. (d) TEM images of porous nano-Si particles with P-dopant. (e) P concentration, conductivity, and porosity of nano-Si particles produced by different weight ratios of Si to P_2O_5 . (f) and (g) EDS mapping of the porous nano-Si particles with P-dopant after acid-etching. (h) Cycling performance of porous nano-Si particles with P dopant, prepared from different weight ratios of Si to P_2O_5 . (i) Cycling performance of porous nano-Si particles with P-dopant produced by different weight ratios of Si to P_2O_5 . (j) Cycling performance at different rates from 0.05 to 5C of porous nano-Si particles with P-dopant produced by different weight ratios of Si to P_2O_5 . Reproduced with permission.⁵¹ Copyright 2022 ACS publication. (k) Illustration of the fabrication process of tubular SiO_xC_y . Reproduced with permission.⁴⁹ Copyright 2019 Elsevier.

enhancing the fracture toughness of the material. This modification effectively constrains dislocation movement by exploiting the solute-strengthening mechanism. As a result, the material can possess excellent structural stability during cycling. Moreover, the diffusion rate of electrons and lithium ions in Ge is much higher than that of Si materials. Consequently, the anode has excellent cycling performance and capacity retention; after 80 cycles at 0.5 A g^{-1} , the material retains a discharge capacity of 1210 mA h g^{-1} (Fig. 12d). At a high current density of 1.6 A g^{-1} , the capacitance retention rate of 300 cycles can come up to 70% (Fig. 12e). While Ge metal is relatively expensive, it also exhibits poor stability and is

susceptible to external environmental factors, which consequently adversely impacts the battery's performance.⁵⁴

Gao *et al.* fused Sn, Sb, and silicon within an arc furnace to craft a uniform alloy ingot. Subsequently, they employed high-energy ball milling to promote an intimate bonding among these metals, ultimately yielding a nanomaterial characterized by a multiphase interwoven structure with an average particle diameter of 38 nm, as shown in SEM and TEM images (Fig. 12f and g). In XRD and HRTEM images, the average grain size of 38 nm can be obtained after doping (Fig. 12h and i). The resultant silicon anode material through this innovative process exhibits a network structure induced by the doping of Sn

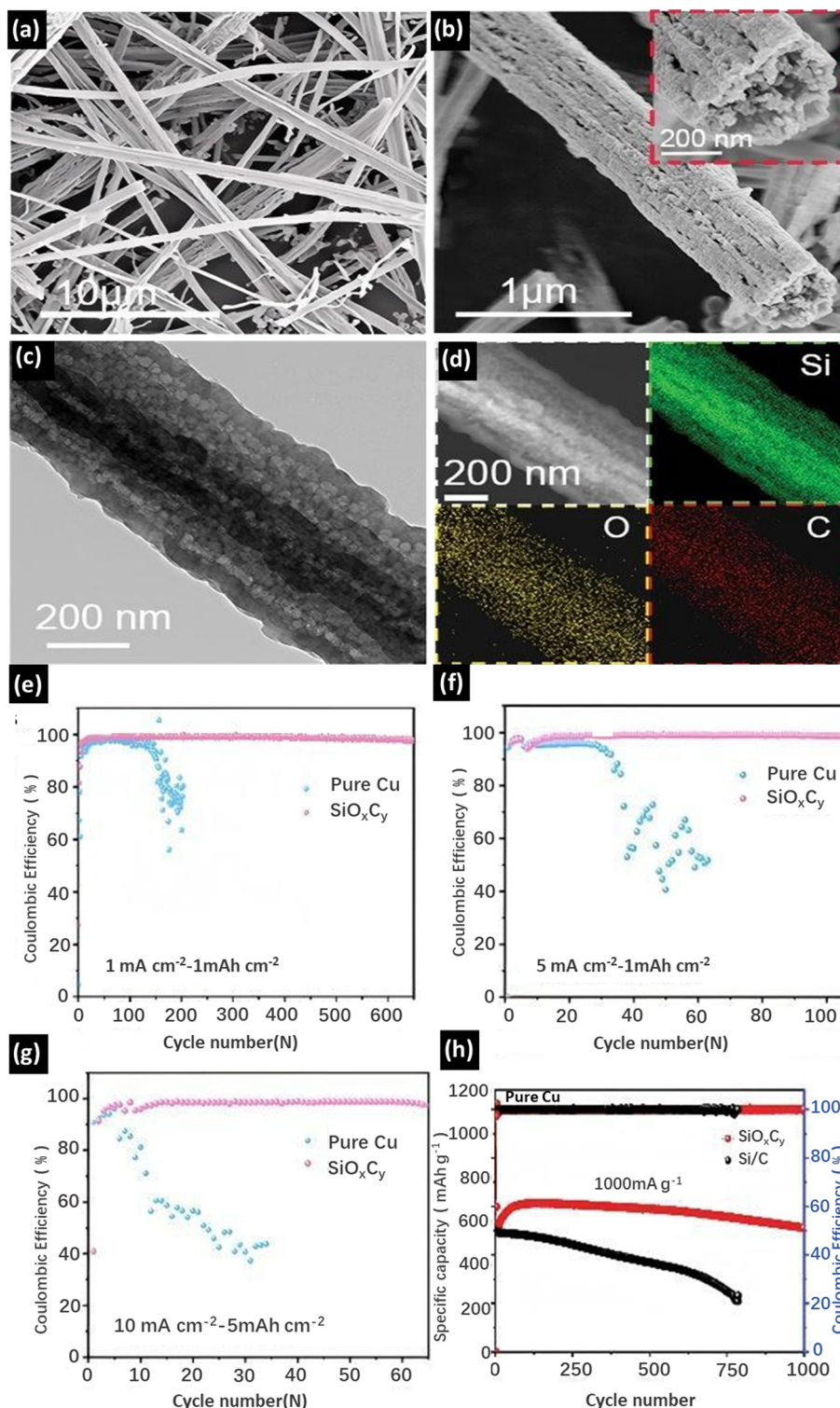


Fig. 10 (a) and (b) SEM images of SiO_xC_y . (c) TEM images of SiO_xC_y . (d) EDS mapping of SiO_xC_y . (e) Coulombic efficiency of Li plating/stripping on SiO_xC_y and Cu foil collectors at changing current densities at 1.0 mA cm^{-2} with a fixed capacity of 1.0 mA h cm^{-2} . (f) Coulombic efficiency of Li plating/stripping on SiO_xC_y , and Cu foil collectors at 5.0 mA cm^{-2} at 5.0 mA h cm^{-2} . (g) Coulombic efficiency of Li plating/stripping on SiO_xC_y , and Cu foil collectors at 10.0 mA cm^{-2} with a fixed capacity of 5.0 mA h cm^{-2} . (h) Long cyclability of SiO_xC_y and commercial Si/C at 1000 mA g^{-1} . Reproduced with permission.⁴⁹ Copyright 2023, John Wiley and Sons.

and Sb. This distinctive architecture significantly accelerates the diffusion rate of lithium ions and elevates electronic

conductivity. Moreover, the addition of elements can cause the lattice distortion of Si and destroy the long-range ordered

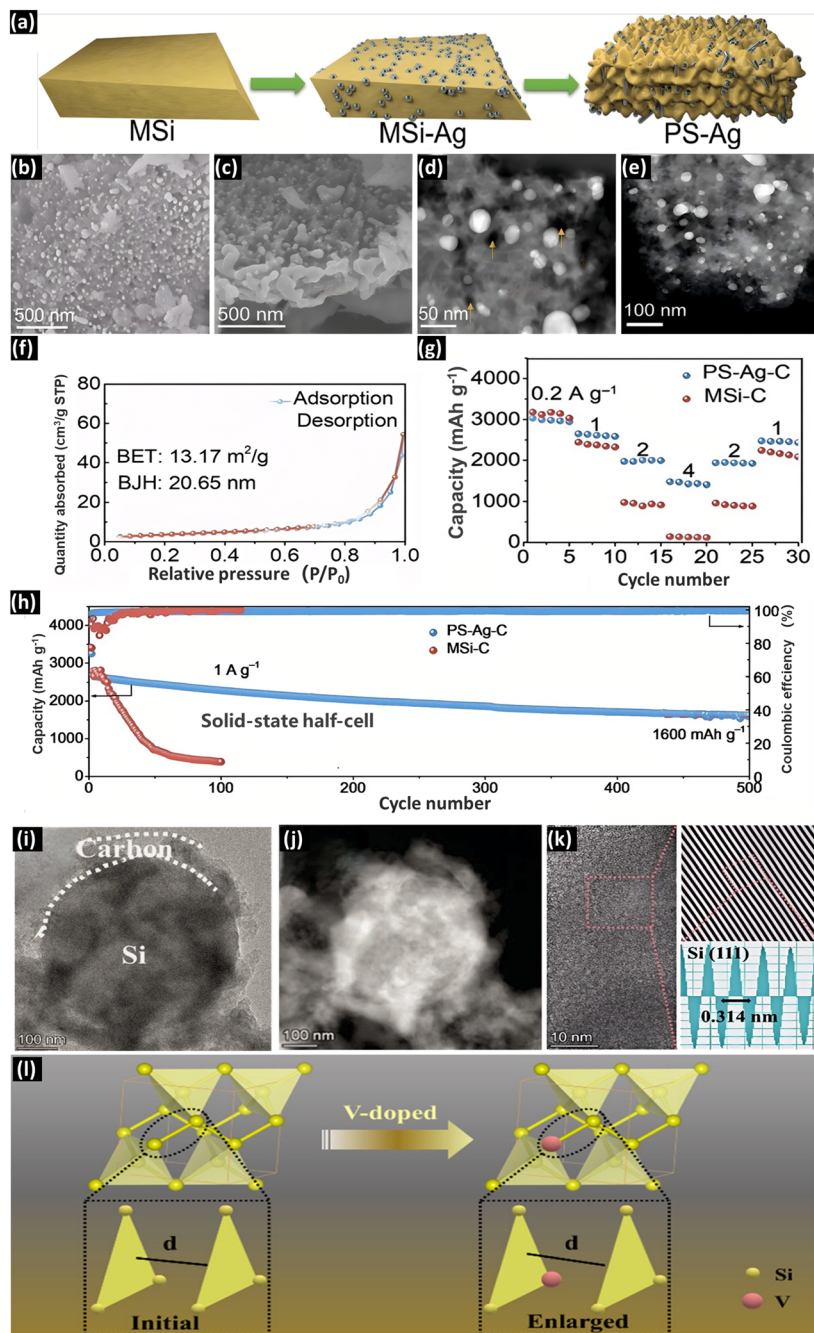


Fig. 11 (a) The schematic illustration of the synthesis process of PS-Ag particles via an Ag assisted wet chemical etching method. (b) Surface SEM image of the surface of PS-Ag particles. (c) Cross-sectional SEM image of PS-Ag particles. (d) TEM image of PS-Ag particles. (e) HAADF-TEM image of PS-Ag and the corresponding elemental mappings of Si-K and Ag-L. (f) BET analysis of PS-Ag powders. (g) The rate capability of PS-Ag-C and MSi-C anodes in solid-state batteries. (h) Long-term cycling performance comparison of PS-Ag-C and MSi-C anodes in solid-state batteries. Reproduced with permission.⁵² Copyright 2023 Royal Society of Chemistry publication. (i) TEM image of V-Si@C-1. (j) HAADF image of V-Si@C-1. (k) High-resolution TEM image of V-Si@C-1. (l) Mechanism diagram of V doping. Reproduced with permission.⁵³ Copyright 2022 ACS publication.

structure, thus hindering the occurrence of two-phase reactions, and the smoother voltage curves measured also prove that the reactions are more similar to solid solution reactions, which helps to alleviate stress concentration and improve battery stability. The discharge capacitance of the Sn and

Sb co-doped material at 100 cycles at 1 A g^{-1} and 3 A g^{-1} was 1.62 A h g^{-1} and 1.19 A h g^{-1} , with capacity retention rates of 99.86% and 99.88%, respectively (Fig. 12j).⁵⁵

Information from the recent studies is summarized in Table 4; in general, the doping of other elements into the

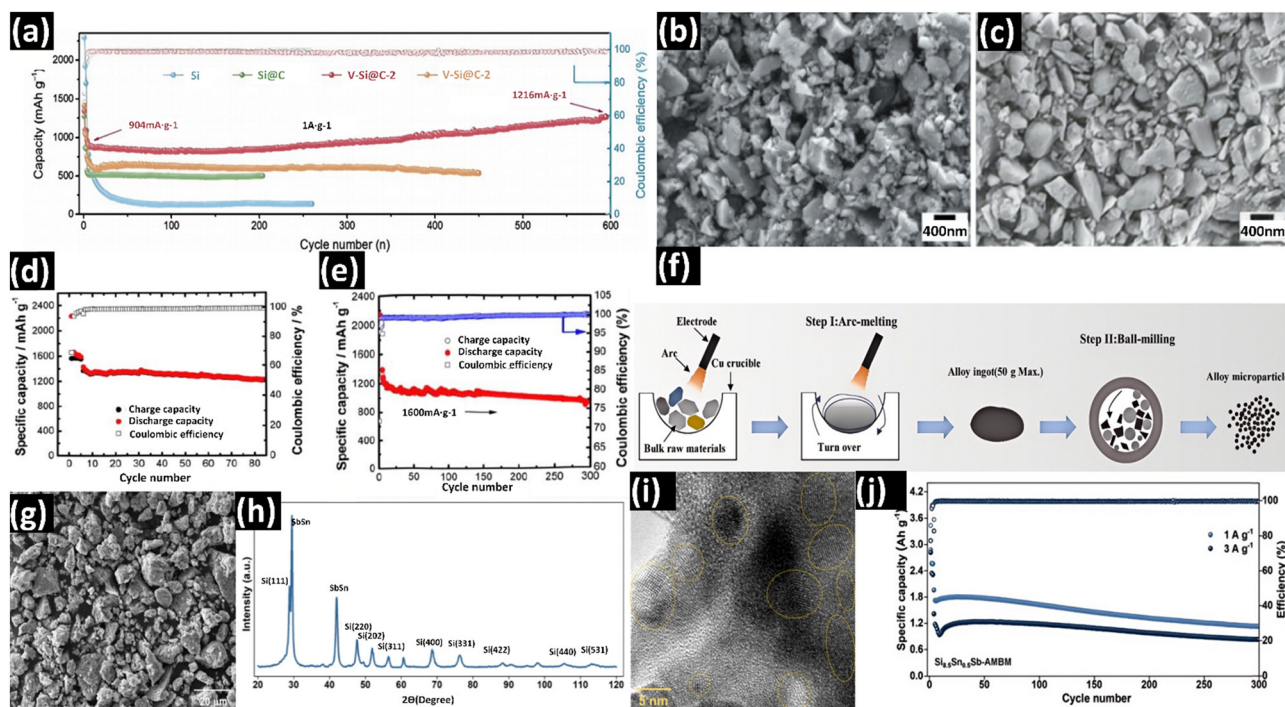


Fig. 12 (a) Long cycle performance at 1 A g^{-1} of different electrodes. (b) SEM images of $\text{Si}_{0.50}\text{Ge}_{0.50}$. (c) SEM images of $\text{Si}_{0.75}\text{Ge}_{0.25}$. (d) Cyclic capacity performance of $\text{Si}_{0.50}\text{Ge}_{0.50}$. (e) Cyclic capacity performance of the $\text{Si}_{0.50}\text{Ge}_{0.50}$ electrode at the current density of 1600 mA g^{-1} , after 5 formation cycles at 200 mA g^{-1} . Reproduced with permission.⁵⁴ Copyright 2018 Springer Nature. (f) Illustration of combining arc-melting and high energy ball milling to prepare concentration modulated Si-rich ($\text{Si}_{8.5}\text{Sn}_{0.5}\text{Sb}$) microparticles. (g) SEM image of $\text{Si}_{8.5}\text{Sn}_{0.5}\text{Sb}$. (h) Granularity statistics of $\text{Si}_{8.5}\text{Sn}_{0.5}\text{Sb}$. (i) HRTEM image of prepared microparticles. (j) Cycling performance of the $\text{Si}_{8.5}\text{Sn}_{0.5}\text{Sb}$ -AMB anode at 1 and 3 A g^{-1} . Reproduced with permission.⁵⁵ Copyright 2023 Springer Nature.

crystal lattice of silicon at a microscopic size leads to the formation of more defects, which provide more active sites for the intercalation of Li ions and enhance the ability of Si to contain Li ions in the alloying reaction, especially for some metal elements, such as Ag, Sn, V, and Ge, which could not merely initiate the generation of lattice strain, but provide extra capacity (1600 mA h g^{-1} for Ge, 1000 mA h g^{-1} for Sn); therefore, doping in Si at the atomic scale has become a promising strategy for the challenges of Si anodes in LIBs.

Silicon composites

Volume expansion during silicon lithiation is unavoidable, so researchers have tried to combine Si with other materials as anodes to address this challenge. For instance, researchers tried to form a film with high mechanical strength and iron conductivity on the surface of Si, forming a unique core-shell structure to inhibit the volume expansion of Si, and also formed a small amount of stable SEI outside the shell to provide anode activity; compounding Si with a highly conductive binder also inhibits the expansion of Si. We'll explain that in more detail below.^{1,3,4,7,56–61}

To alleviate volume expansion of Si, the simplest and most intuitive method is to coat Si with high-strength materials, which generate interfacial stress when Si expands, preventing further volume expansion without limiting the transport of lithium ions and the silicon-lithium alloying reaction. In

addition, existing studies have shown that certain materials can promote the generation of high-strength SEI away from the internal Si, which is beneficial for the activity of the anode. However, the thickness, strength and other functions of the cladding layer are difficult to control, which challenges the processing method. Consequently, we not only summarize the effective cladding materials but also give a detailed description of their preparation process and provide suggestions on the improvement strategy.^{62–66}

Leicheng Zhang *et al.* successfully synthesized Si@ metal-organic framework (MOF) composites paired with fiber-supported polyethylene oxide (PEO) garnet composite electrolyte (PPG) solid electrolyte, for the modification of Si nanoparticles *via* a facile hydrothermal method followed by calcination. The synthesis of Si@ZIF-67 involves mixing polyvinylpyrrolidone (PVP) with ethanol, into which silicon nanoparticles were introduced. Subsequently, the resulting mixture is left to stir and then reintroduced into a solution containing cobalt(II) nitrate hexahydrate and 2-methylimidazole. After heating and being isolated, the precursor is subjected to calcination under an argon atmosphere at 800°C for 2 hours, yielding the final Si@MOF product. Si nanoparticles are incorporated within a microscale carbon host derived from MOFs, which efficiently accommodates the large-volume changes during cycling while facilitating sufficient charge transfer pathways. In the SEM TEM and EDS images, the morphology of the

Table 4 Silicon anode doped with different elements and its electrochemical properties

Si-based anode	Electrolyte	Initial CE	Specific capacity (mA h g ⁻¹)	Current density (mA g ⁻¹)	Initial discharge capacity (mA h g ⁻¹)	Ref.
Si _{0.5} Ge _{0.5}	Fluoroethylene carbonate (1 : 1)	70.05%	1210 (80 cycles)	500	2228.4	54
PS-Ag-C	PVDF-HFP/LATP SSE	89.60%	1610 (500 cycles)	200	3030.3	52
Si _{8.5} Sn _{0.5} Sb	LiPF ₆	82.62%	1620 (100 cycles)	100	~2000	55
V-Si@C	LiPF ₆	73.52%	1216 (600 cycles)	1000	904	53
SiO _x (x < 0.1)	Argyrodite-type sulfide SE	75.40%	2600 (50 cycles)	~141	2500	27
NGF-Si	LiPF ₆	99.32%	2031 (200 cycles)	298	~3450	50
Si with P-dopant	LiPF ₆	85.4%	1500 (940 cycles)	1C	~3500	51
SiO _x C _y	LiPF ₆	—	580 (1000 cycles)	1000	~700	49

as-synthesized Si@MOF is observed, which is successfully encapsulated within a carbon host derived from ZIF-67, exhibiting a conformal polyhedral structure (Fig. 13a–c). The PPG was fabricated by integrating PEO and garnet-type Li_{6.5}La₃Zr_{1.5}Ta_{0.5}O₁₂ (LLZTO) into the PVDF fiber skeleton, which indicates that the garnet fillers are well dispersed, enhancing ionic conductivity within the electrolyte (Fig. 13d). Furthermore, the cycling examinations reveal the presence of cracks and voids within the bare Si electrode and at the electrode/PPG interface. In contrast, the Si@MOF electrode demonstrates mitigated volume expansion and maintains a well-preserved interface without signs of detachment. This is attributed to the MOF-derived carbon host, which effectively constrains the repeated deformation of Si nanoparticles, thus significantly enhancing interfacial stability towards the excellent reversibility of PPG (Fig. 13e and f). The Si@MOF electrode which showcases decent electrochemical performance with a high initial CE of 72.0% delivers an initial capacity of 1967 mA h g⁻¹, which is lower than that of the bare Si (2646 mA h g⁻¹), at a current density of 200 mA g⁻¹ and exhibits a high reversible capacity of 1442 mA h g⁻¹ compared with the bare Si electrode

(636 mA h g⁻¹) after 50 cycles (Fig. 13g). Using the full battery using the LiFePO₄ (LFP) cathode, the Si@MOF electrode with a high ICE of 71.6% delivers a high initial specific capacity of ~135 mA h g⁻¹ and retains 73.1% of its original capacity after 500 cycles at 0.5C (Fig. 13h–j). However, composite materials need to be heat treated at 800 °C which may increase energy consumption.⁶⁷

Dongcan Zhang *et al.* employed a thermal chemical vapor deposition (CVD) approach to growing vertical graphene (VG) sheets on commercial Si nanoparticles and thus synthesized fabricated Si@VG nanocomposites for polymer all-solid-state battery (ASSB) anodes. The synthesis of Si@VG involves introducing Si nanoparticles into a tubular furnace, and then subjecting them to a temperature ramp under an argon atmosphere and then introducing methane and hydrogen maintained at a particular temperature. This heat treatment process facilitated the formation of the Si@VG product. From the SEM images, the vertical growth of graphene sheets on Si nanoparticle surfaces through the CVD process was observed at varying magnifications, resulting in the formation of Si@VG, each approximately 200 nm in size (Fig. 14a and b). The TEM images

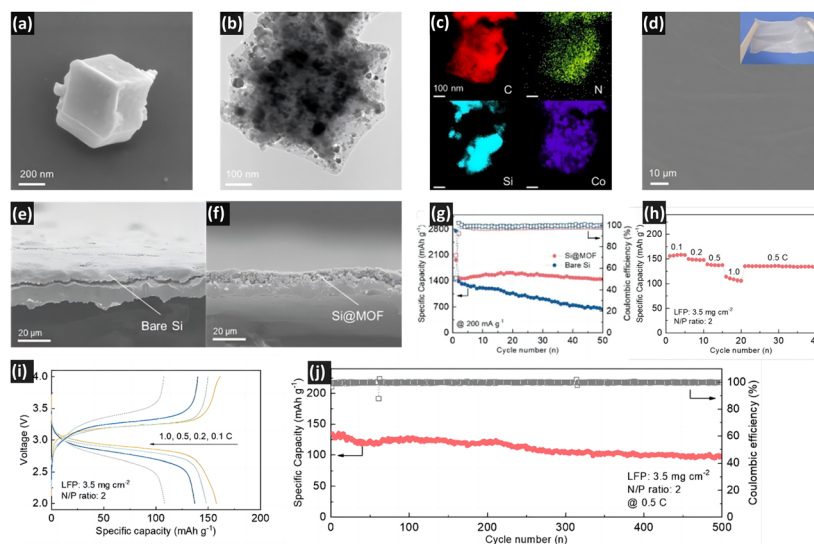


Fig. 13 (a) SEM and (b) TEM images of the Si@MOF structure and corresponding (c) EDS elemental mapping results of C, N, Si, and Co. SEM images of PPG from the (d) top and cross-sectional SEM images of (e) bare Si and (f) Si@MOF anodes after cycles. (g) Lithiation capacities of Si@MOF and bare Si electrodes at 200 mA g⁻¹. (h) Discharge capacities and (i) voltage profiles of the Si@MOF full cell at 0.1, 0.2, 0.5, and 1.0C. (j) Cycling stability of the Si@MOF full cell at 0.5C for 500 cycles. Reproduced with permission.⁶⁷ Copyright 2022 ACS publication.

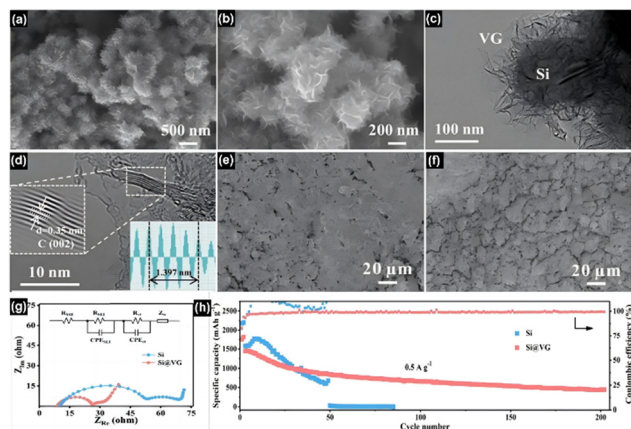


Fig. 14 (a) and (b) SEM images of Si@VG. (c) and (d) TEM images of Si@VG. (e) SEM images of Si@VG after 200 cycles. (f) SEM images of Si after 50 cycles. (g) EIS impedance spectra of Si@VG and Si. (h) Cycling performance of Si@VG and Si. Reproduced with permission.⁶⁸ Copyright 2022 ACS publication.

further reveal that some graphene nanosheets on the surface are thin, bending, well-dispersed and cross-linked, forming a network structure, which enhances interconnectivity with other nanosheets, significantly enhancing the electrical conductivity across the entire electrode. Enhancing the compatibility between vertical graphene nanosheets and polymer solid electrolytes to reduce interfacial impedance, improving their suitability of the vertical graphene nanosheets with the polymer solid electrolyte for reducing interfacial impedance (Fig. 14c and d). From the SEM images of pure Si, noticeable cracks are observed on the electrode surface after 50 cycles, resulting in a loss of electrical contact and a rapid decline in capacity. In contrast, the Si@VG composite maintains a distinct particle morphology with no significant cracks observed on the electrode surface after 200 cycles, which can be attributed to the restraining effect of the vertical graphene sheets on the volume expansion of Si (Fig. 14e and f). Furthermore, EIS measurements reveal a substantial reduction in the interfacial impedance between the anode and the solid polymer electrolyte (Fig. 14g). As the anode for ASSBs, Si@VG with a high ICE of 83.4% delivers an initial capacity of 1442.6 mA h g⁻¹, which is lower than that of the bare Si (1600 mA h g⁻¹), at 0.5 A g⁻¹ and exhibits a reversible capacity of 444.9 mA h g⁻¹ after 200 cycles. In contrast, the pure Si electrode suffers from significant capacity decay and fails abruptly after only 50 cycles, highlighting the superior cycling stability of the Si@VG composite (Fig. 14h).⁶⁸

Han *et al.* synthesized MgO-coated silicon powder through the heat treatment of micron-sized Si and Mg(NO₃)₂·H₂O. They then incorporated a carbon framework *via* polyacrylonitrile (PAN) to produce Si@MgO@C particles (Fig. 15a). XRD images indicate the successful deposition of MgO on the surface (Fig. 15c). Additionally, SEM images reveal the successful synthesis of carbon and the embedding of silicon particles within the carbon network, which provide an efficient conductive pathway to facilitate electron transport (Fig. 15d). Insights

from theoretical simulations further demonstrate that the stress in the Si@MgO@C material is predominantly released in the vicinity of the MgO coating. Notably, this structure reduces the stress value from 30 GPa to 20 GPa and also minimizes the relative increase in diameter (Fig. 15b and e). These findings confirm that the MgO coating effectively mitigates volume expansion and enhances structural stability during cycling. In solid-state batteries, when operated at a current density of 0.05 A g⁻¹, the anode exhibits a remarkable specific capacity of 3224.6 mA h g⁻¹ (Fig. 15f). Even after undergoing 100 cycles at 0.3 A g⁻¹, the specific capacity remains at 1658.9 mA h g⁻¹ (Fig. 15g). The MgO coating successfully alleviates volume expansion; however, a pronounced capacity decay is observed in the prolonged cycling tests. The image indicates a noticeable downward trend in the long-term cycling performance. Under long-term application conditions, the coating may progressively deteriorate due to mechanical stress, ultimately impacting the overall stability of the material.⁶⁹

The abovementioned coating layer is not active towards lithium-ion transport. Although the volume expansion is suppressed, the kinetics of lithiation/delithiation may be affected. Hence the ionic conductor coating is also developed.

Xiao Xu *et al.* synthesized a sheet-type Si anode for sulfide based all-solid-state lithium batteries (ASSLBs) (Si@LiAlO₂) *via* conventional slurry coating methods, possessing high mechanical strength, high ionic conductivity, superior cycle performance and high rate performance. The process of synthesizing Si@AlO₂ involves coating a layer of Al₂O₃ on Si nanoparticles *via* a scalable solution-based approach, whose thickness is precisely controlled by the quantity of Al sulfate and reaction time. Especially, the weight of Al sulfate is employed at either 1.2 g or 1.6 g while the reaction time is set at 0.5 hours in this research. To further enhance the ionic conductivity of the Al₂O₃ coating layer, LiOH·H₂O is introduced to react with Al₂O₃ to obtain the ionic conductor LiAlO₂ and thus synthesize a sheet-type Si anode Si@LiAlO₂. The XRD patterns showcase that all the Si@LiAlO₂ specimens exhibit typical characteristics of crystalline Si with no other peaks observed, attributed to the thin thickness and amorphous nature of the LiAlO₂ coating layer (Fig. 16b). The TEM images of Si@LiAlO₂ particles illustrate an amorphous layer with a thickness of 2–3 nm which was homogeneously coated on Si (Fig. 16c and d). According to the SEM images, the uncoated Si and Si@LiAlO₂ anodes show thicknesses of 10.0 and 8.3 μm, respectively. After 51 cycles, the two electrodes exhibited thicknesses of 13.9 and 9.5 μm, which are 39.0% and 14.5% thicker than the initial value (Fig. 16e and f). The smaller thickness change demonstrates that Si@LiAlO₂ with high mechanical strength can accommodate the large-volume changes during cycling. Using all-solid-state half-cells, the Si@LiAlO₂ electrode with a high initial CE over 80% delivers an initial capacity of 1890 mA h g⁻¹, which is lower than that of the uncoated Si (2646 mA h g⁻¹), at a rate of 0.33C and exhibits a high specific capacity of 1164 mA h g⁻¹ compared with the uncoated Si electrode (696 mA h g⁻¹) after 150 cycles. This is attributed to the improved Li⁺ diffusion kinetics in the electrodes and less expansion ratio of the

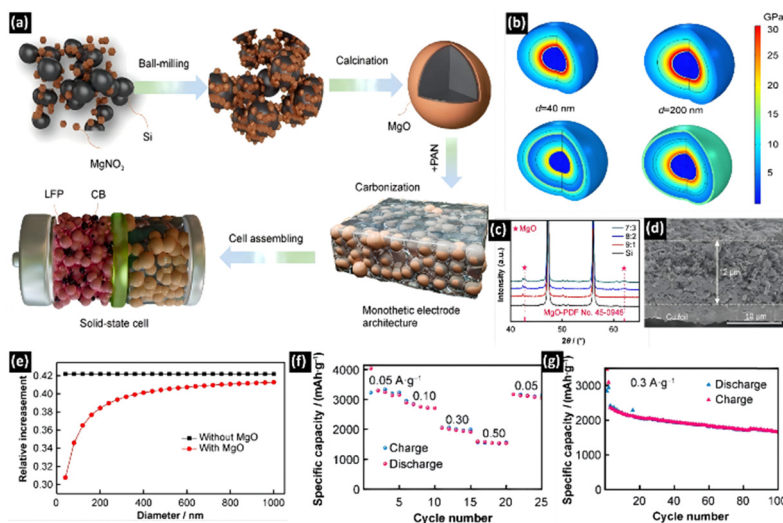


Fig. 15 (a) Schematic illustration of the synthesis process and potential advantages. (b) Modelling and stress distribution of both Si particle and Si@MgO particle with diameters of 40 nm and 200 nm. (c) XRD patterns of pristine Si powders and Si@MgO with different mass ratios of 9:1, 8:2 and 7:3. (d) Cross-sectional SEM image of the Si@MgO@C anode. (e) Relative increment of Si and Si@MgO versus diameter. (f) Rate performance of the Si@MgO@C anode tested in SSBs. (g) Long-term cycling performance of the Si@MgO@C anode at 0.3 A g⁻¹ and 0.5 A g⁻¹. Reproduced with permission.⁶⁹ Copyright 2023 Springer Nature.

electrode (Fig. 16g). The Si@LiAlO₂/NCM@LNO all-solid-state full-cell with a high ICE of 71.6% delivers a high reversible specific capacity of 147.7 mA h g⁻¹ after 150 cycles at 0.33C and a considerable capacity retention of 80.2% after 62 cycles at 2.8 mA cm⁻² (Fig. 16h). However, the interface stability, in ASSLBs, between the silicon anode and the sulfide electrolyte is a challenge, as the high reactivity between silicon and sulfide

electrolytes may lead to lithium dendrite growth and short-circuiting.⁷⁰

Gu *et al.* mixed micro silicon (MSi), LiOH, and NH₄H₂PO₄ by ball milling, and subjected them to heat treatment to create the SiO₂/Li₃PO₄ (LPO) ionic conductive layer on the silicon surface. Following microwave-assisted heating, Si@SiO₂@LPO@C composite materials were obtained (Fig. 17a). TEM images revealed

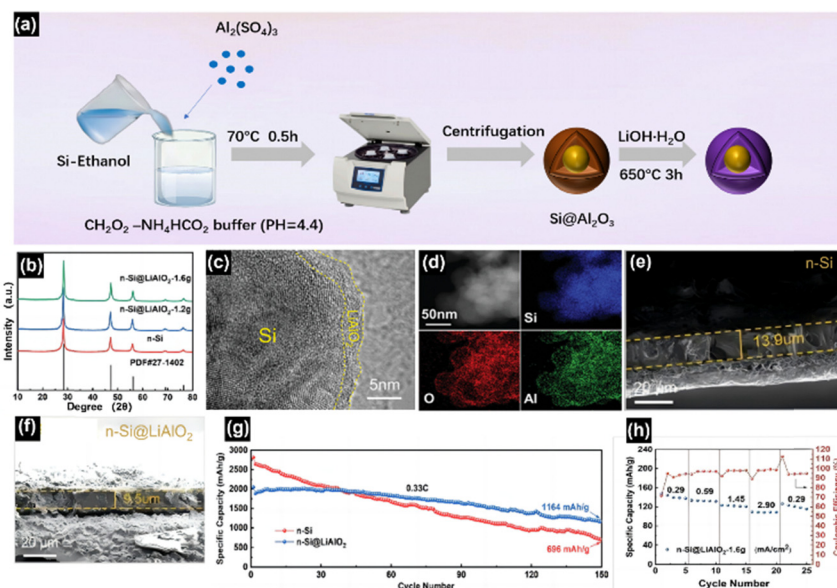


Fig. 16 (a) XRD patterns of Si and Si@LiAlO₂ powders. (b) HR-TEM images of Si@LiAlO₂. (c) High-angle annular dark-field (HAADF) images of Si@LiAlO₂ and elemental mapping images of Si, O, and Al. (d) and (e) Cross-sectional images of Si and Si@LiAlO₂ after cycling for 51 cycles. (f) Cycle performance of Si and Si@LiAlO₂ in all-solid-state half-cells at 0.33C. (g) Rate performance at 0.29, 0.58, 1.45, and 2.9 mA cm⁻². Reproduced with permission.⁷⁰ Copyright 2023 John Wiley and Sons.

that the LPO layer ranged in thickness from 12.5 to 25.4 nm, while the SiO_2 layer measured approximately 2 nm (Fig. 17c–e). By analyzing HADDF-STEM images and the corresponding elemental maps, it was evident that the conductive shell was evenly coated onto the Si particles (Fig. 17f). XPS images further confirmed the successful synthesis of both LPO and SiO_2 (Fig. 17g). The presence of Si–O and P–O bonds allows the diffusion of lithium ions by way of jumping within the electrode, significantly enhancing lithium-ion transport rates. Moreover, during the cycling process of the solid-state battery, a highly mechanically stable and uniform SEI layer formed on the electrode surface, effectively mitigating stress generated during cycling. Even after volume expansion, this layer ensured that battery capacity remained largely unchanged, contributing to the battery's excellent kinetic performance (Fig. 17b). Consequently, in a solid-state battery operating at 1 A g^{-1} , the $\text{Si@SiO}_2\text{@LPO@C}$ electrode exhibited a reversible specific capacity of $2482.1 \text{ mA h g}^{-1}$, with an initial coulombic efficiency of 88.7%. After 80 cycles, the anode maintained a specific capacity of $1441.0 \text{ mA h g}^{-1}$ (Fig. 17h). However, this material has shortcomings in settling the inherent interfacial contact problem of solid-state batteries, resulting in a performance that is somewhat less than optimal compared to liquid batteries utilizing the same electrodes.⁷¹

Xu *et al.* proceeded by adding nano-silicon, Li_2S , and P_2S_5 powder to acetonitrile (ACN), followed by thorough stirring and mixing. After drying to eliminate the solvent, heat treatment was conducted to obtain Si@LPS anode materials (Fig. 17i). The HRTEM image reveals that $\text{Li}_7\text{P}_3\text{S}_{11}$ (LPS) is uniformly coated

onto the Si surface, forming a shell layer approximately 5–10 nm thick (Fig. 17j). The STEM-EDS elemental map further confirms the even distribution of the cladding material's elements, indicating a successful and effective coating (Fig. 17k). Notably, the solid-state battery electrolyte they prepared is also LPS, which significantly addresses the issue of poor interface contact in solid-state batteries. This facilitates rapid lithium-ion diffusion and the formation of a highly stable SEI film, effectively inhibiting volume expansion during the lithiation/delithiation process. Additionally, LPS exhibits excellent electrical conductivity, promoting the efficient transport of electrons and lithium ions. Under a current density of 50 mA g^{-1} , the Si@LPS electrode exhibits an initial charge capacity of $1049.9 \text{ mA h g}^{-1}$, retaining $904.8 \text{ mA h g}^{-1}$ after 35 cycles, with a capacity retention rate of 86.2%, demonstrating remarkable cycling stability (Fig. 17l). From the data, it is evident that the electrochemical performance of the material has not undergone significant enhancement. This may indicate that the coating is unable to fully address the issues of expansion and low conductivity associated with the silicon anode.⁷²

In conclusion, we have made a comprehensive analysis of the coating of Si and focused on the coating material, the characteristics of the coating structure and the production process of the coating layer.^{73–77} The relevant data can be found in Table 5. Critically, despite showing compromised performance in restraining volumetric expansion and mitigating silicon fragmentation when benchmarked against rigid materials, engineered coatings featuring either high Young's modulus or autonomous repair mechanisms provide distinct advantages

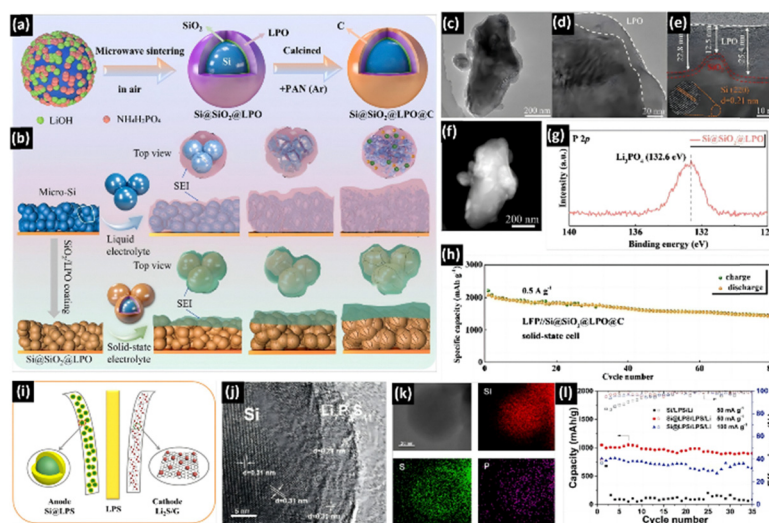


Fig. 17 (a) The synthesis process of the $\text{Si@SiO}_2\text{@LPO@C}$ material. (b) Schematic illustrating that $\text{Si@SiO}_2\text{@LPO@C}$ enhances the mechanical stability and provides a fast Li/electron transport pathway, and that PEO/LiTFSI contributes to a stable SEI layer mainly comprising LiF. The robust mechanical structure and the stable SEI layer synergistically lead to a high-performance micron-Si anode. (c) and (d) TEM image and (e) high-resolution TEM image of the $\text{Si@SiO}_2\text{@LPO}$ particle. (f) HADDF TEM image of the $\text{Si@SiO}_2\text{@LPO}$ particle and the corresponding elemental mapping of Si, O, and P. (g) XRD patterns of the P 2p XPS spectra of the $\text{Si@SiO}_2\text{@LPO}$ particle and Si. (h) The cycling performance of $\text{Si@SiO}_2\text{@LPO@C}$ in a full solid-state cell with an LFP cathode. Reproduced with permission.⁷¹ Copyright 2022 Elsevier. (i) Schematic of the structure of the all-solid-state $\text{Li}_2\text{S/Si}$ battery with LPS solid electrolyte; the cathode consists of Li_2S and graphene, and the anode contains silicon coated with a LPS solid electrolyte layer. (j) HRTEM image of Si@LPS . (k) STEM EDS elemental mapping images of Si@LPS , marked by the rectangle region, for Si, S, and P. The charge/discharge voltage profiles of all solid-state half-batteries. (l) Cycling performances of Si and Si@LPS at a rate of 50 mA g^{-1} and Si@LPS at a rate of 100 mA g^{-1} at room temperature. Reproduced with permission.⁷² Copyright 2022 Springer Nature.

through: (i) effective conservation of electrical percolation networks among nano-scale fracture fragments, and (ii) consequent enhancement of interfacial charge transfer and long-term electrode integrity.^{78,79} Considering that coated Si is an efficient modification method, the commercial coating process is of particular significance, while the effective coating methods in the laboratory (sol-gel coating, atomic layer deposition (ALD), *etc.*) are unrealistic to be applied on a large scale in the industry due to high cost or strict condition requirements; consequently, low-cost coating methods such as plasma method, molten salt method and so on will become the focus of future coating process research. However, the tendency of Si to expand causes strong stresses at the interface, which might lock the Si lattice locally, affecting the transport of lithium ions in the Si lattice. To solve this problem, creating a proper void between Si and the coating material to allow proper Si expansion may also further release the capacity potential of Si, which requires more imaginative processes.^{80–85}

Conclusions

Si has become the most promising anode material for further development of the potential of solid-state lithium-ion batteries.^{72,86–94} On the one hand, Si provides a capacity far beyond that of conventional graphite anodes, which is conducive to the expansion of battery capacity, and on the other hand, compared with the lithium metal anode, Si itself is a more stable substance, and there are fewer possibilities to produce lithium dendrites, which affect the cycle life of the battery, so solving the application challenge of Si anodes in solid-state batteries will trigger a breakthrough in the lithium battery field.⁹⁵ As shown in Fig. 19, in recent years, the modification

of the Si anode and exploration of its application in solid-state lithium-ion batteries have become a hot spot of interest for researchers, and the number of high-level papers has continued to increase in recent years, which also proves the importance and hotness of this field, so our summary in this field is necessary and critical (Fig. 18).

In this article, we introduce the necessity of applying silicon to solid-state lithium-ion batteries and the challenges associated with this, due to the electrochemical-mechanical behavior of silicon in cycles, such as amorphization and electrochemical sintering, volume expansion and the cracking and pulverization of Si. Accordingly, we have summarized three strategies: the design of the Si nanostructure, doping different elements in the silicon lattice, and the preparation of mesoscopic-scale Si composites.

For silicon, although the expansion stress is unavoidable during the lithiation reaction, the volume expansion effect can be mitigated by the special structural design of pure silicon: the nano-sized silicon has a significant reduction in stress due to the larger specific surface area, and the design of nanoparticles, nanofilms, and nanoporous structures further counteracts stress and alleviates volume expansion. At the same time, the existence of a certain degree of amorphous state is beneficial, increasing Young's modulus of silicon and producing a lower level of deformation after stress, which usually requires the doping of different elements in crystalline silicon to cause lattice distortion. In addition, forming a protective layer around silicon to limit volumetric expansion is an effective method, which has high requirements for the conductivity and mechanical properties of the coating material.^{5,30,96–99}

It is predicted that future developments can focus on the following strategies:

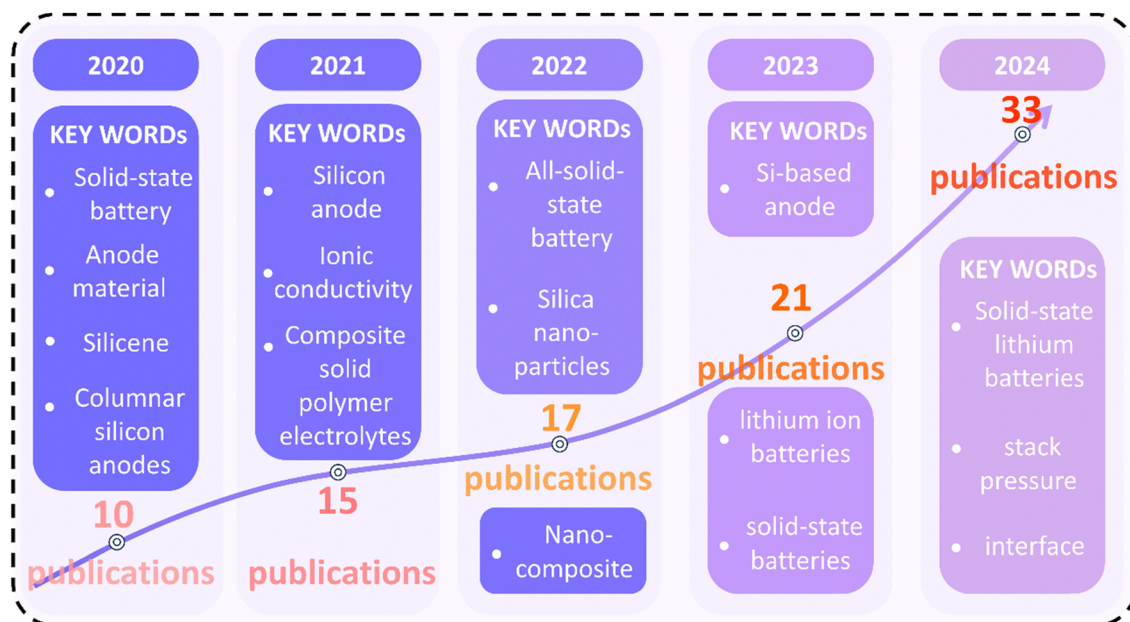


Fig. 18 Number of publications on Si anodes in SSBs in the last five years.

Table 5 Preparation method and performance of the silicon composite anode

Si-based anode	Method	Electrolyte	ICE	Specific capacity (mA h g ⁻¹)	Current (mA g ⁻¹)	Initial capacity (mA h g ⁻¹)	Ref.
Si@ZIF-67	A facile hydrothermal	PPG	72.0%	1442 (50 cycles)	200	1967	67
Si@VG	Thermal CVD	PEO	83.4%	444.9 (200 cycles)	500	1442.6	68
Si@MgO@C	Heat treatment	PEO/LATP/NCF	—	1658.9 (100 cycles)	300	2844.1	69
Si@LiAlO ₂	Slurry coating	Li ₆ PS ₅ Cl	80.1%	1164 (150 cycles)	0.33C	1890	70
Si@SiO ₂ @LPO@C	Ball milling and heat treatment	PEO/LiTFSI	93.8%	1425.0 (80 cycles)	500	2074.4	71
Si@LPS	Heat treatment	Li ₇ P ₃ S ₁₁	—	904.8 (35 cycles)	50	1049.9	72

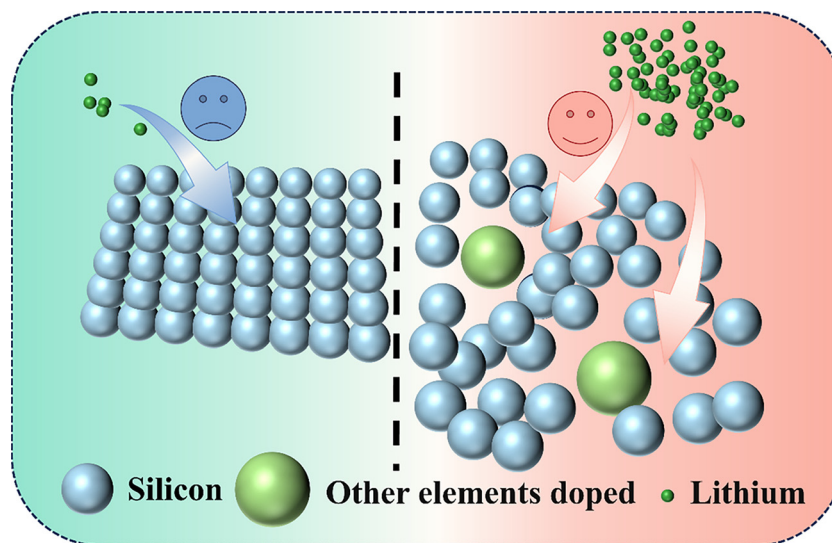


Fig. 19 The doping of other elements causes lattice distortion, which provides more sites for the lithiation reaction.

(1) Doping other elements to increase lattice defects and lithium-ion combining sites, as atoms of different sizes are doped into the Si lattice, lattice distortion and more dangling bonds are generated, which is conducive to enhancing the strength of the anode material to resist deformation and providing more sites for lithium intercalation, and if the doped atoms can react with lithium ions, the capacity density can be further improved, so doping is a promising strategy to improve the silicon anode of lithium-ion solid-state batteries. As shown in Fig. 19, atoms of different sizes (green) cause larger local lattice gaps (blue represents Si), providing more sites for the lithiation reaction and significantly increasing the capacity of the anode. In addition, doping can cause local stresses and improve mechanical properties. Element doping can significantly influence the electrochemical performance of silicon (Si) as an anode material for lithium-ion batteries, encompassing capacity, cycling stability, and rate capability. The specific effects depend on the type and concentration of the dopant elements, as well as the resulting structural/electronic modifications. Doping with non-metallic elements such as carbon (C), nitrogen (N), and boron (B) can enhance the conductivity of Si and improve capacity retention; for instance, B introduces hole carriers and facilitates Li⁺ diffusion within Si. Tin (Sn), on the

other hand, can form alloys with Si, thereby improving long-term structural stability while contributing additional capacity due to its lithium storage capability. However, it should be noted that doping with lithium-inactive elements (*e.g.*, Cu) may dilute the specific capacity of the Si anode. Excessive doping of certain elements (*e.g.*, B > 5 at%) could also block Li⁺ transport pathways. Therefore, *in situ* XRD/XAS studies are recommended to investigate the lithiation behavior of doped Si and guide the optimization of doping strategies.

(2) Limit the level of lithiation of Si to achieve the effect of lithium metal batteries, so that lithiation and lithium plating are carried out at the same time, breaking the upper limit of Si capacity, that is to achieve the behavior of the silicon anode of the lithium metal battery in the lithium-ion battery. Moreover, under the dual action of lithiation and lithium plating, the current at the interface is more uniform, which means that the deposition of lithium ions is also more uniform, which greatly reduces the risk of lithium dendrite formation, avoiding dendrite puncture of the separator after multiple cycles, which results in instability or short circuits of the battery. As illustrated in Fig. 20, the liquid electrolyte maintains uniform contact with the silicon anode in conventional lithium-ion batteries, establishing an isotropic chemical potential (μ_{Li^+})

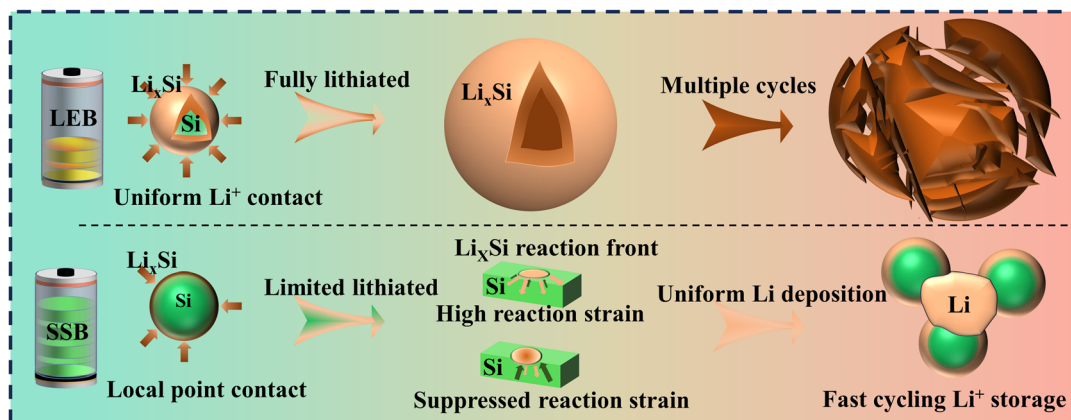


Fig. 20 The different behavior of Si in LEBs and SSBs: only the lithiation reaction occurs in LEBs, while in SSBs, the lithiation reaction and lithium plating occur synergistically to produce uniform lithium deposition.

distribution. This homogeneous environment enables simultaneous lithiation across the entire outer surface of Si particles. The resulting alloying-induced volume expansion occurs uniformly in all directions, causing stress fields to mutually cancel. Consequently, this stress equilibrium state presents minimal resistance to lithium-ion diffusion into the silicon matrix. The lithiation reaction spreads rapidly, making the entire Si particle rapidly lithiated, so the silicon anode often exhibits a great irreversible volume expansion (usually $>300\%$) and destruction, causing poor cycle performance, while in all solid-state electrolyte batteries, due to the local point-to-point contact between the solid electrolyte and Si particles, the alloying reaction between Si and lithium and volume expansion will only occur at the surface contact site, and due to the uneven lithiation sites, a stress field will be generated inside the Si particles, which will cause strain contraction at the front of the lithiation reaction, limit the further diffusion of lithium ions inward, and prevent the lithiation reaction of internal Si particles. As a result, the silicon particles maintain a low level of lithiation and have low volume expansion, without swelling

and cracking, causing excellent cycling performance. At the same time, at the local lithiation site on the silicon surface, lithium ions combine with electrons, forming lithium metal deposited in the voids between the silicon particles (lithium plating), which provides additional capacity and lays the foundation for rapid cycling of the battery.^{100,101} Luhan Ye *et al.* have further proposed the concept of constriction-susceptible anode materials, and in lithium-ion solid-state batteries, the self-limiting lithiation behavior of silicon enables surface-selective lithium incorporation, thereby maintaining the bulk material at low lithiation states. Concurrently, reversible lithium metal plating/stripping compensates for the limited silicon lithiation, synergistically providing enhanced capacity and exceptionally high Coulombic efficiency. It is worth noting that they reported that through this idea, a specific capacity of more than 5000 mA h g^{-1} can be achieved, providing a solution strategy for further improving the energy density of lithium-ion batteries.¹⁰²

(3) Form a proper coating of Si materials, and to achieve the purpose of inhibiting the expansion of the negative electrode

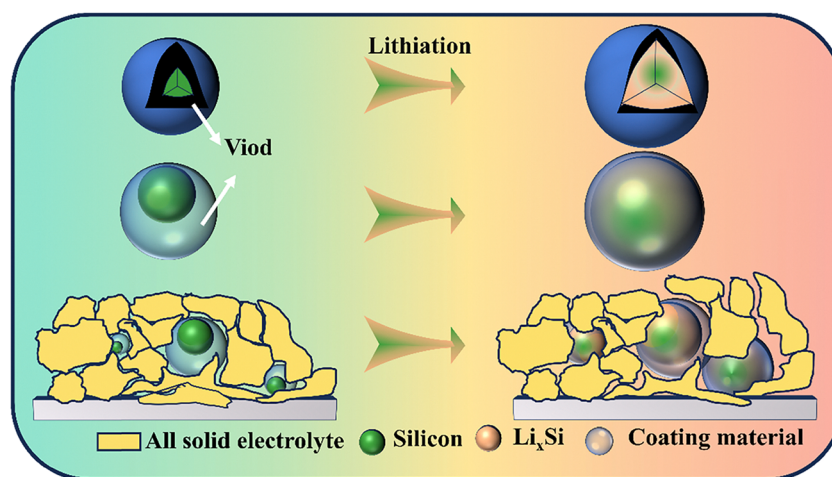


Fig. 21 The voids used for buffering can release stress, and this hollow structure could increase the lifetime of Si and facilitate the contact between Si and solid electrolyte during the reaction.

and relieving stress at the same time, without hindering the diffusion of lithium ions in the crystal lattice: forming an appropriate gap between Si and the rigid coating layer or using a more ductile coating material. As shown in Fig. 21, there exists a gap between the coating material and Si to relieve the stress caused by Si expansion, and the synergy between the void and the outer material ensures that the Si particles have a sufficient lifespan, which significantly improves the cycling stability of the battery.

For silicon-based composite materials, it is essential to not only investigate the application of coating strategies but also to design self-healing binders (e.g., those incorporating dynamic covalent bonds or hydrogen-bonding networks) as buffering structures to accommodate the volumetric changes of silicon. Drawing inspiration from pre-lithiation techniques applied to silicon anodes in liquid electrolyte batteries, electrochemical pre-lithiation methods can be employed to compensate for lithium loss during the initial cycle, while further exploring their impact on the electrode–solid-state electrolyte interface and potential optimization strategies.

Advanced *in situ* characterization techniques, such as transmission electron microscopy (TEM), X-ray diffraction (XRD), and Raman spectroscopy, should be utilized to observe silicon expansion and solid electrolyte interphase (SEI) evolution. Synchrotron radiation-based methods, including X-ray absorption spectroscopy (XAS), can provide deeper insights into interfacial chemical transformations. Furthermore, molecular dynamics (MD) simulations can elucidate the formation mechanisms of the SEI, while density functional theory (DFT) calculations can reveal reaction dynamics at the silicon–electrolyte interface. Finite element analysis (FEA) should also be applied to optimize stress distribution within the electrode structure, ensuring enhanced mechanical stability and electrochemical performance. This integrated approach, combining material engineering, interfacial modification, and multiscale computational modelling, will contribute to the development of robust silicon-based anodes for next-generation energy storage systems.¹⁰³

In summary, although there are many difficulties, the use of silicon anodes in solid-state batteries is the general trend, and we hope that our review can provide a reference for the future application of silicon anodes.

Author contributions

C. Han: conceptualization, funding acquisition, resources, supervision, visualization, writing – review & editing. Y. Deng: conceptualization, data curation, funding acquisition, visualization, writing – original draft. X. H. Feng: data curation, investigation, visualization, writing – original draft. Z. L. Qian: data curation, investigation, visualization, writing – original draft. J. R. Ma: data curation, investigation, visualization, writing – original draft. Y. T. OuYang: investigation, resources, supervision.

Data availability

No primary research results, software or code have been included and no new data were generated or analysed as part of this review.

Conflicts of interest

The authors declare that they have no conflict of interest.

Acknowledgements

C. Han acknowledges the financial support from the National Natural Science Foundation of China (Grant No. 52204378). Y. Deng acknowledges the financial support from the Natural Science Foundation of Hunan Province (Grant No. 2024JJ10017).

References

- 1 K. Hu, J. Chen and J. Zhang, *Energy Storage Mater.*, 2025, **75**, 104029.
- 2 Y. Li, H. Yang and F. Qin, *Mater. Today Commun.*, 2025, **43**, 111578.
- 3 M. N. Naseer, J. S. Sevillano and M. Fehse, *J. Energy Storage*, 2025, **111**, 115334.
- 4 H. Zhang, J. Li and Y. Zhu, *J. Alloys Compd.*, 2025, **1013**, 178554.
- 5 E. Balamoorthy, M. Selvaraj and M. Pahuja, *Chem. Eng. J.*, 2025, **505**, 159110.
- 6 R. Kumar, A. L. Sharma and R. K. Singh, *Chem. Phys. Impact*, 2025, **10**, 100814.
- 7 C. R. Lee, M. Kim and C. Hwang, *Nanoscale*, 2025, **17**, 2852–2859.
- 8 L. Sun, Y. Liu and L. J. Wang, *Adv. Funct. Mater.*, 2024, **34**, 2403032.
- 9 D. Chen, M. Hong and J. Wan, *React. Funct. Polym.*, 2025, **207**, 106130.
- 10 O. Sheng, T. Jin and T. Wang, *Small*, 2024, e2409680.
- 11 Z. Wang, Y. Xia and T. Mao, *Chem. Eng. J.*, 2025, **503**, 158438.
- 12 L. Braks, J. Zhang and A. Förster, *Angew. Chem., Int. Ed.*, 2024, **63**, e202408238.
- 13 P. C. Li, Z. Q. Zhang and Z. W. Zhao, *Angew. Chem., Int. Ed.*, 2024, **63**, e202319090.
- 14 X. L. Wang, Y. Li and J. Liu, *Angew. Chem., Int. Ed.*, 2025, **64**, e202421101.
- 15 P. Zhao, Y. Zhang and B. Sun, *Angew. Chem., Int. Ed.*, 2024, **63**, e202317016.
- 16 A. K. Mishra, J. Parmarand and I. Mukhopadhyay, *J. Energy Storage*, 2024, **87**, 111421.
- 17 H. A. Lee, M. Shin and J. Kim, *Adv. Mater.*, 2021, **33**, e2007460.
- 18 M. Z. Ge, C. Y. Cao and G. M. Biesold, *Adv. Mater.*, 2021, **33**, 2004577.
- 19 Q. Y. Wang, M. Zhu and G. R. Chen, *Adv. Mater.*, 2022, **34**, e2109658.

- 20 S. Y. Pan, J. W. Han and Y. Q. Wang, *Adv. Mater.*, 2022, **34**, e2203617.
- 21 D. Kim, S. Chin and S. H. Jeong, *Energy Storage Mater.*, 2025, **76**, 104136.
- 22 Y. Mari, T. Yoshihiro and S. Atsushi, *J. Power Sources*, 2020, **473**, 228595.
- 23 B. A. Farshad, A. Parnaz and M. A. Ali, *Adv. Funct. Mater.*, 2024, **34**, 2314822.
- 24 B. Q. Chen, D. M. Xu and S. M. Chai, *Adv. Funct. Mater.*, 2024, **34**, 2401794.
- 25 L. Wang, J. J. Lu and S. Y. Li, *Adv. Funct. Mater.*, 2024, **34**, 2403574.
- 26 Z. Cheng, W. Chen and Y. Zhang, *Adv. Funct. Mater.*, 2024, **34**, 2408145.
- 27 R. Ohta, T. Hiraoka and Y. Shibano, *J. Phys. D: Appl. Phys.*, 2024, **57**, 255501.
- 28 H. Liu, Q. Sun and H. Zhang, *Energy Storage Mater.*, 2023, **55**, 244–263.
- 29 Q. Sun, G. F. Zeng and X. Xiao, *Adv. Energy Mater.*, 2024, **14**, 2470176.
- 30 J. Z. Chen, S. G. Wang and Y. L. Hou, *J. Energy Storage*, 2023, **74**, 109356.
- 31 A. M. Li, Z. Wang and T. P. Pollard, *Nat. Commun.*, 2024, **15**, 1206.
- 32 Q. Wu, X. Luo and L. Zhou, *Next Mater.*, 2025, **7**, 100390.
- 33 Y. Ni, S. B. Tu and R. M. Zhan, *Trans. Tianjin Univ.*, 2022, **29**, 101–109.
- 34 Z. P. Li, L. Ze and Z. H. Ma, *J. Alloys Compd.*, 2024, **971**, 172738.
- 35 Y. Zhou, W. Feng and Y. Xu, *Eng. Sci.*, 2023, **28**, 1060.
- 36 M. Chiku, N. Kitade and C. Hotehama, *Electrochim. Acta*, 2024, **505**, 144963.
- 37 Y. Zhang, H. Chang and A. Han, *J. Alloys Compd.*, 2024, **983**, 173919.
- 38 O. Ryota, Y. Mari and K. Atsutaka, *Electrochem. Commun.*, 2022, **138**, 107288.
- 39 X. Li, L. Zhang and Y. Fan, *Chin. Chem. Lett.*, 2025, **36**, 109776.
- 40 R. Qiao, X. Shen and C. Mao, *Nano Lett.*, 2024, **24**, 15629–15637.
- 41 S. Jing, Y. Lu and Y. Huang, *Adv. Mater.*, 2024, **36**, e2312305.
- 42 J. Kim, C. Kim and I. Jang, *J. Power Sources*, 2021, **510**, 230425.
- 43 C. L. Wang, H. F. Jiu and L. X. Zhang, *J. Alloys Compd.*, 2023, **956**, 170332.
- 44 B. V. BhaskaraRao, D. P. Pabba and R. Aepuru, *J. Mater. Sci.: Mater. Electron.*, 2023, **34**, 1910.
- 45 S. S. Wei, Q. Z. Chen and R. L. Zhu, *Appl. Clay Sci.*, 2024, **254**, 107388.
- 46 R. Okuno, M. Yamamoto and Y. Terauchi, *Energy Procedia*, 2019, **156**, 183–186.
- 47 R. DeWees, A. Thapaand and M. Sunkara, *ACS Appl. Mater. Interfaces*, 2025, **17**, 3742–3748.
- 48 M. C. Zhao, J. Zhang and C. M. Costa, *Adv. Mater.*, 2023, **36**, e2308590.
- 49 S. Z. Fan, S. Q. Cui and J. Q. Zhang, *Small*, 2023, **19**, e2304290.
- 50 S. J. Yeom, T. Wi and S. Ko, *ACS Appl. Mater. Interfaces*, 2022, **14**, 5237–5246.
- 51 G. X. Lv, B. Zhu and X. Q. Li, *ACS Appl. Mater. Interfaces*, 2017, **9**, 44452–44457.
- 52 X. Han, L. Gu and Z. Sun, *Energy Environ. Sci.*, 2023, **16**, 5395–5408.
- 53 H. Luo, X. M. Zhang and Z. Y. Wang, *ACS Appl. Mater. Interfaces*, 2023, **15**, 4166–4174.
- 54 K. Mishra, X.-C. Liu and M. Geppert, *J. Mater. Res.*, 2018, **33**, 1553–1564.
- 55 Y. Gao, L. Fan and R. Zhou, *Nano-Micro Lett.*, 2023, **15**, 222.
- 56 K. N. Joo, K. M. Seon and P. J. Hyun, *Energy Storage Mater.*, 2024, **64**, 103074.
- 57 J. Pan, H. Lu and D. Wu, *Energy Storage Mater.*, 2024, **72**, 103701.
- 58 W. B. Huang, Y. Wang and L. Z. Lv, *Energy Storage Mater.*, 2023, **60**, 102837.
- 59 L. Yang, T. Meng and W. Zheng, *Energy Storage Mater.*, 2024, **72**, 103766.
- 60 R. Ye, J. Liu and J. Tian, *ACS Appl. Mater. Interfaces*, 2024, **16**, 16820–16829.
- 61 W. Zhang, W. Li and S. Gui, *ACS Appl. Mater. Interfaces*, 2024, **16**, 26234–26244.
- 62 Y. Liu, J. Duan and P. Li, *Chem. – Asian J.*, 2024, **20**, e202400838.
- 63 Q. Ai, Q. Fang and J. Liang, *Nano Energy*, 2020, **72**, 104657.
- 64 W. Y. Song and O. B. Chae, *Batteries*, 2024, **10**, 327.
- 65 S. Yoo, J.-I. Lee and S. Ko, *Nano Energy*, 2013, **2**, 1271–1278.
- 66 M. Zhang, N. Bai and W. Lin, *J. Alloys Compd.*, 2025, **1010**, 177012.
- 67 L. Zhang, Y. Lin and X. Peng, *ACS Appl. Mater. Interfaces*, 2022, **14**, 24798–24805.
- 68 D. Zhang, P. Yu and Y. Zhang, *ACS Appl. Energy Mater.*, 2023, **7**, 726–734.
- 69 H. Xiang, X. Min and G. L. Hui, *Rare Met.*, 2023, **43**, 1017–1029.
- 70 X. Xu, Q. Sun and Y. Y. Li, *Small*, 2023, **19**, e2302934.
- 71 L. H. Gu, J. J. Huan and M. F. Chen, *Energy Storage Mater.*, 2022, **52**, 547–561.
- 72 X. Xu, J. Cheng and Y. Li, *J. Solid State Electrochem.*, 2019, **23**, 3145–3151.
- 73 M. A. Firdaus, N. H. Hawari and C. G. Adios, *Chem. – Asian J.*, 2024, **19**, e202400036.
- 74 W. S. Eun, K. DoHoon and K. M. Ji, *Nanomaterials*, 2022, **13**, 132.
- 75 M. A. Firdaus, N. H. Hawari and C. G. Adios, *Chem. – Asian J.*, 2024, **19**, e202400036.
- 76 K. K. Heon, N. M. Gyun and K. M. Jun, *Carbon*, 2023, **210**, 118056.
- 77 J. Xiao, J. W. Han and D. B. Kong, *Energy Storage Mater.*, 2022, **50**, 554–562.
- 78 W. Kang, Q. Zhang and Y. Jia, *J. Power Sources*, 2024, **602**, 234338.

- 79 L. J. Wen, Y. Wan and C. X. Jin, *J. Energy Storage*, 2023, **73**, 108835.
- 80 M. Liu, A. Song and X. Y. Wang, *Nano Energy*, 2025, **136**, 110749.
- 81 Z. Qi, J. Chen and Z. Yi, *Carbon*, 2024, **224**, 119074.
- 82 X. Tan, Z. Zhao and Z. Na, *RSC Adv.*, 2024, **14**, 11323–11333.
- 83 L. Wang, J. Yu and S. Li, *Energy Storage Mater.*, 2024, **66**, 103243.
- 84 W. B. Huang, Y. Wang and L. Z. Lv, *Energy Storage Mater.*, 2022, **52**, 646–654.
- 85 H. Zhang, R. Hu and Y. Liu, *Energy Storage Mater.*, 2018, **13**, 257–266.
- 86 S. Lee, K. S. Oh and J. E. Lee, *J. Energy Chem.*, 2025, **105**, 243–251.
- 87 A. M. Skundin and T. L. Kulovas, *Russ. J. Electrochem.*, 2025, **60**, 1228–1242.
- 88 S. Cangaz, F. Hippauf and F. S. Reuter, *Adv. Funct. Mater.*, 2020, **10**, 2001320.
- 89 R. Huang, R. Li and S. Li, *Chem. Eng. J.*, 2025, **503**, 158154.
- 90 J. Kim, J. Jeong and D. Lee, *Chem. Eng. J.*, 2025, **505**, 159328.
- 91 C. Li, Y. Wu and F. Ren, *Small*, 2025, e2411451.
- 92 P. Molaiyan, B. Boz and G. S. D. Reis, *eTransportation*, 2025, **23**, 100391.
- 93 D. L. Nelson, S. E. Sandoval and J. Pyo, *ACS Energy Lett.*, 2024, **9**, 6085–6095.
- 94 S. E. Sandoval, C. G. Haslam and B. S. Vishnugopi, *Nat. Mater.*, 2025, 1–9.
- 95 A. K. Stephan, *Joule*, 2021, **5**, 3074–3075.
- 96 S. Casino, P. Niehoff and M. Börner, *J. Energy Storage*, 2020, **29**, 101376.
- 97 M. B. Naikwade, P. K. Katkar and S. W. Lee, *Ceram. Int.*, 2024, **50**, 54778–54790.
- 98 M. Yang, J. Liu and S. Li, *Nano Energy*, 2019, **65**, 104028.
- 99 Y. Zhang, Y. Zhang and Q. Deng, *J. Energy Storage*, 2024, **81**, 110483.
- 100 Y. Deng, Y. Ouyang and C. Han, *Chin. J. Struct. Chem.*, 2024, **43**, 100276.
- 101 J. Gui, Z. Huang and J. Lu, *Carbon Neutralization*, 2025, **4**, e182.
- 102 L. Ye, Y. Lu and Y. Wang, *Nat. Mater.*, 2024, **23**, 244–251.
- 103 Y. Mu, R. Ma and S. Xue, *Carbon Neutralization*, 2024, **3**, 4–31.